




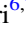














The *Spitzer*-IRAC/MIPS Extragalactic Survey (SIMES). II. Enhanced Nuclear Accretion Rate in Galaxy Groups at $z \sim 0.2$

I. Baronchelli^{1,2,3} , G. Rodighiero³ , H. I. Teplitz¹ , C. M. Scarlata² , A. Franceschini³, S. Berta^{4,21} , L. Barrufet⁵, M. Vaccari^{6,7} , M. Bonato⁷, L. Ciesla⁸, A. Zanella⁹ , R. Carraro^{10,11}, C. Mancini³ , A. Puglisi^{3,9} , M. Malkan¹² , S. Mei^{1,13,14} , L. Marchetti^{5,6,15} , J. Colbert¹, C. Sedgwick⁵, S. Serjeant⁵ , C. Pearson^{5,16,17} , M. Radovich¹⁸, A. Grado¹⁹ , L. Limatola¹⁹ , and G. Covone^{19,20}

¹ IPAC, Mail Code 314-6, Caltech, 1200 E. California Blvd., Pasadena, CA 91125, USA; ivano@ipac.caltech.edu

² MN Institute for Astrophysics, University of Minnesota, 116 Church St. SE, Minneapolis, MN 55455, USA

³ Dipartimento di Fisica e Astronomia, Università di Padova, vicolo Osservatorio, 3, I-35122 Padova, Italy

⁴ University of Zagreb, Physics Department, Bijenička cesta 32, 10002 Zagreb, Croatia

⁵ Department of Physical Sciences, The Open University, Milton Keynes, MK7 6AA, UK

⁶ Department of Physics and Astronomy, University of the Western Cape, Robert Sobukwe Road, Bellville, 7535, South Africa

⁷ INAF—Istituto di Radioastronomia, Via Piero Gobetti 101, I-40129 Bologna, Italy

⁸ Laboratoire AIM Paris-Saclay CEA/IRFU/SAP, Université Paris Diderot, Orme des Merisiers, Building 709, F-91191 Gif-sur-Yvette Cedex, France

⁹ European Southern Observatory, Karl Schwarzschild Straße 2, D-85748 Garching, Germany

¹⁰ Instituto de Física y Astronomía, Universidad de Valparaíso, Gran Bretaña 1111, Playa Ancha, Valparaíso, Chile

¹¹ Department of Astronomy, Yale University, 52 Hillhouse Avenue, New Haven, CT 06511, USA

¹² Department of Physics and Astronomy, UCLA, Physics and Astronomy Bldg., 3-714, Los Angeles, CA 90095-1547, USA

¹³ GEPI, Observatoire de Paris, CNRS, University of Paris Diderot, Paris Sciences et Lettres (PSL), 61, Avenue de l'Observatoire F-75014, Paris, France

¹⁴ University of Paris Denis Diderot, University of Paris Sorbonne Cité (PSC), F-75205 Paris Cedex 13, France

¹⁵ Department of Astronomy, University of Cape Town, Private Bag X3, Rondebosch, 7701, South Africa

¹⁶ RAL Space, Rutherford Appleton Laboratory, Chilton, Didcot, Oxfordshire OX11 0QX, UK

¹⁷ Oxford Astrophysics, Denys Wilkinson Building, University of Oxford, Keble Rd., Oxford OX1 3RH, UK

¹⁸ INAF—Astronomical Observatory of Padua, vicolo dell'Osservatorio 5, I-35122 Padova, Italy

¹⁹ INAF—Osservatorio Astronomico di Capodimonte Via Moiariello 16, I-80131 Napoli, Italy

²⁰ Dipartimento di Fisica, University of Naples Federico II, INFN, Via Cinthia, I-80126 Napoli, Italy

Received 2017 October 2; revised 2018 February 26; accepted 2018 March 15; published 2018 April 16

Abstract

For a sample of star-forming galaxies in the redshift interval $0.15 < z < 0.3$, we study how both the relative strength of the active galactic nucleus (AGN) infrared emission, compared to that due to the star formation (SF), and the numerical fraction of AGNs change as a function of the total stellar mass of the hosting galaxy group (M_{group}^*) between $10^{10.25}$ and $10^{11.9} M_{\odot}$. Using a multicomponent spectral energy distribution SED fitting analysis, we separate the contribution of stars, AGN torus, and star formation to the total emission at different wavelengths. This technique is applied to a new multiwavelength data set in the SIMES field (23 not-redundant photometric bands), spanning the wavelength range from the UV (*GALEX*) to the far-IR (*Herschel*) and including crucial *AKARI* and *WISE* mid-IR observations ($4.5 \mu\text{m} < \lambda < 24 \mu\text{m}$), where the black hole thermal emission is stronger. This new photometric catalog, which includes our best photo- z estimates, is released through the NASA/IPAC Infrared Science Archive (IRSA). Groups are identified through a friends-of-friends algorithm ($\sim 62\%$ purity, $\sim 51\%$ completeness). We identified a total of 45 galaxies requiring an AGN emission component, 35 of which are in groups and 10 in the field. We find the black hole accretion rate (BHAR) $\propto (M_{\text{group}}^*)^{1.21 \pm 0.27}$ and (BHAR/SFR) $\propto (M_{\text{group}}^*)^{1.04 \pm 0.24}$, while, in the same range of M_{group}^* , we do not observe any sensible change in the numerical fraction of AGNs. Our results indicate that the nuclear activity (i.e., the BHAR and the BHAR/SFR ratio) is enhanced when galaxies are located in more massive and richer groups.

Key words: galaxies: evolution – galaxies: groups: general – galaxies: star formation – infrared: galaxies – quasars: supermassive black holes – submillimeter: galaxies

1. Introduction

In the last few years, the study of the nature of active galactic nuclei (AGNs) and their host galaxies has been driven by the discovery of various scaling relations between their physical properties and the way they vary during cosmic time (see Kormendy & Ho 2013 for a review).

Starbursts and AGNs are found to coexist at all redshifts (Farrah et al. 2003; Alexander et al. 2005), showing a similar evolution in terms of global star formation rate density (SFRD; Lilly et al. 1996; Hopkins & Beacom 2006; Burgarella et al. 2013) and black hole accretion rate density (BHARD; Franceschini

et al. 1999; Hopkins et al. 2007a; Merloni & Heinz 2008; Delvecchio et al. 2014), with a rise through $z \sim 2$ and a consecutive fall after that epoch. The masses of supermassive black holes (SMBHs) and the bulge of their host galaxies show a tight correlation (Marconi & Hunt 2003; Vika et al. 2012; Läscher et al. 2014), while the BHAR is related to the stellar mass M^* (Mullaney et al. 2012; Rodighiero et al. 2015) through a relation similar to the so-called “main sequence” of star-forming galaxies existing between the SFR and M^* (Brinchmann et al. 2004; Daddi et al. 2007; Elbaz et al. 2007; Noeske et al. 2007b; Rodighiero et al. 2014; Aird et al. 2017a). Finally, Gruppioni et al. (2016) and Rodighiero et al. (2015) found the BHAR to increase at larger SFR and specific SFR (sSFR = SFR/ M^*).

²¹ Visiting Scientist.

The correlations found between the properties of AGNs and their host galaxies suggest that a secular coevolution must have been in place during cosmic time. The possible self-regulation of the AGN–host galaxy systems, possibly driven by AGN-feedback mechanisms, has been often invoked as an explanation for these correlations (e.g., Madau et al. 1996; Granato et al. 2004; Springel et al. 2005b; Farrah et al. 2012; Page et al. 2012), even if a complete explanation of the phenomenon remains unclear, at least at lower stellar masses (Fiore et al. 2017). Recently, Aird et al. (2017b) found stochastic processes to be primarily responsible for the fueling of AGNs and their variability.

Complicating the picture here summarized, the environment in which galaxies are located plays an important role in their evolution. In the local universe, star formation seems more likely to happen in less dense environments, such as small groups or in the field, rather than in more massive clusters, but the SFR in cluster galaxies increases strongly with redshift (e.g., Butcher & Oemler 1984; Poggianti et al. 2006; Saintonge et al. 2008). AGNs are influenced by the environment as well. At low redshifts, the fraction of galaxies hosting X-ray-identified AGNs is lower among cluster galaxies than in the field (Gisler 1978; Dressler et al. 1985; Hill & Oegerle 1993; Dressler et al. 1999; Kauffmann et al. 2004; Rines et al. 2005; Popesso & Biviano 2006). Quiescent galaxies, typically populating the inner regions of galaxy clusters, are also observed to host weaker AGNs than star-forming galaxies (Aird et al. 2017b). However, the fraction of AGNs inside clusters is evolving with z more rapidly than in the field (Eastman et al. 2007; Martini et al. 2009, 2013). Similarly, the AGN duty cycle for both quiescent and star-forming galaxies evolves strongly with redshift and becomes comparable at $z \sim 2$ (Aird et al. 2017b). The mechanism thought to be responsible for the concomitant activation of star formation and central BH accretion, at least for the most X-ray-luminous sources, is a large gas infall due to major mergers (Sanders et al. 1988; Barnes & Hernquist 1991; Hopkins et al. 2006). In general, the dense environment of the cluster can influence the galaxy activity through different mechanisms, such as minor mergers, harassment, ram-pressure stripping, and strangulation (e.g., Gunn & Gott 1972; Richstone 1976; Larson et al. 1980; Sanders et al. 1988; Kawata & Mulchaey 2008; McCarthy et al. 2008; van den Bosch et al. 2008; Park & Hwang 2009).

In this framework, the study of dusty star-forming galaxies and accreting SMBHs is crucial. At the peak of the cosmic star formation history, most of the ultraviolet (UV) light emitted by massive young stars and absorbed by the dusty star-forming regions is reemitted at longer wavelengths, with a peak at $\sim 100 \mu\text{m}$ (e.g., Kirkpatrick et al. 2012). This is the far-infrared (far-IR) regime recently explored by space telescopes such as *Spitzer* (24–160 μm) and *Herschel* (~ 60 –500 μm). The activity of the central BH can also be heavily obscured. As for the star formation, the dust-enshrouded BH accretion is observable at mid-IR wavelengths. In this spectral region, the dusty torus surrounding the accretion disk of an SMBH reemits the highly energetic flux from the central engine absorbed at short wavelengths. The *AKARI* and *WISE* observatories allowed us to sample the spectral region interested by the peak of the AGN emission, thanks to their sensitivity at 7, 11, and 15 μm .

In the first part of this work, we present a new set of optical and mid-IR observations covering the central square degree of the *Spitzer*-IRAC/MIPS Extra-galactic Survey (SIMES) field

(see Baronchelli et al. 2016a and references therein). In the second part, we discuss a spectral energy distribution (SED) fitting technique applied to the complete data set spanning the spectral range from the UV (*GALEX*) to the far-IR (*Spitzer*, *Herschel*) wavelengths and the results obtained. The technique used allows us to constrain the optical emission due to stars and disentangle the contribution of the AGN torus and star formation to the total IR luminosity using a triple-component fit. With this approach, we computed stellar masses (M^*), SFRs, and BHARs for the galaxies in our analysis sample. In our analysis, we studied the relations between the properties of the far-IR detected AGNs with their grouping properties.

Our approach is similar to that used in other works (Delvecchio et al. 2014; Gruppioni et al. 2016), but the strength of the data set presented in this paper is the presence of *AKARI* and deep *WISE* mid-IR observations. The *AKARI* data cover only a fraction of the square degree explored in our analysis (the green square in Figure 2; see also Table 1). However, the *WISE* observations, covering the entire sky and being particularly deep close to the south ecliptic pole (SEP), where the SIMES field is located, allow us to constrain the peak of the SMBH IR emission for almost all of the sources in our analysis sample ($0.15 < z < 0.3$; see Figure 1). Following the AGN unified model (Urry & Padovani 1995), a relevant fraction of the high-energy radiation produced in the inner regions of an SMBH is absorbed by the surrounding dusty torus and then reemitted by the heated dust in the far-IR region of the spectrum. For this reason, the IR-based selection of AGNs allows us to mitigate the incompleteness problem (20%–50%) usually affecting X-ray surveys (Donley et al. 2005; Guainazzi et al. 2005; Park et al. 2010; Alexander et al. 2011; Georgantopoulos et al. 2013; Wilkes et al. 2013).

The paper is organized as follows. In Section 2, we present the new set of optical (CTIO, VST) and mid-IR (*AKARI*) observations covering the central region of the SIMES field and complementing the *Spitzer*/IRAC, MIPS, and *Herschel*/SPIRE data described in Baronchelli et al. (2016a, 2016b). In Section 3, we describe the SED fitting technique used to compute photometric redshifts and the method used to improve the precision of our results on 24 μm selected sources through the use of an optical prior. In Section 4, we present the friends-of-friends algorithm used to identify group candidates in the optically covered area. In Section 5, the triple-component SED fitting technique is described, together with the physical quantities obtained for each galaxy in our analysis sample. Finally, in Section 6, we present the results of our analysis of the environmental dependency of the SMBH activity.

Throughout this paper, unless differently specified, we assume AB magnitudes, a Chabrier (2003) initial mass function (IMF), and a standard cosmology with $H_0 = 70 \text{ km s}^{-1} \text{ Mpc}^{-1}$, $\Omega_M = 0.3$, and $\Omega_\Lambda = 0.7$. In the analysis, the quantities not indicated with an underscored “group” refer to single galaxies (e.g., M^* , BHAR, SFR, and bolometric AGN fraction). In contrast, quantities indicated with an underscored “group” refer to the properties of the hosting group (e.g., M_{group}^*). The numerical fractions of AGNs identified in groups and in the field are indicated with f_{group} and f_{field} , respectively.

2. Data

The multiwavelength data collection used in our analysis is based on the deep *Spitzer*/IRAC 3.6 μm observations of the SIMES field, described in Baronchelli et al. (2016a, 2016b);

Table 1
SIMES Field Data Included in the Multiwavelength Catalog

Band	λ_{eff}^a	Instrument/ Telescope	Overlap Area (deg ²)	1σ Depth (μJy)	Used/Required for the AGN Analysis
FUV	154.2 nm	<i>GALEX</i>	2.34	1.27 μJy	Used
NUV	227.4 nm	<i>GALEX</i>	2.34	1.33 μJy	Used
<i>u</i>	355.5 nm	CTIO	0.67	0.89 μJy	Used ^b
<i>B</i>	433.6 nm	CTIO	0.67	0.47 μJy	Used ^b
<i>V</i>	535.5 nm	CTIO	0.66	0.22 μJy	Used ^b
<i>I</i>	793.7 nm	CTIO	0.66	0.24 μJy	Used ^b
<i>R_c</i> ^c	642.8 nm	WFI	1.13	0.18 μJy	Used ^b
<i>g</i>	476.7 nm	VST	1.20	0.059 μJy	Used ^b
<i>i</i>	757.9 nm	VST	1.17	0.18 μJy	Used ^b
<i>z</i>	890.1 nm	VST	1.20	0.31 μJy	Used ^b
<i>J</i> ^d	1.246 μm	VISTA	7.74	1.76 μJy	Used
<i>H</i> ^d	1.631 μm	VISTA	7.74	2.44 μJy	Used
<i>K_s</i> ^d	2.134 μm	VISTA	6.01	5.31 μJy	Used
<i>I1</i> ^c	3.508 μm	IRAC	7.74	1.93 μJy	Required
<i>I2</i> ^c	4.437 μm	IRAC	7.26	1.75 μJy	Used
N3	3.130 μm	<i>AKARI</i>	0.48 (A)	3.2 μJy	Not used (IRAC 3.6 μm instead)
N4	4.251 μm	<i>AKARI</i>	0.48 (A)	2.7 μJy	Not used (IRAC 4.5 μm instead)
S7	6.954 μm	<i>AKARI</i>	0.46 (A)	13 μJy	Used
S11	10.19 μm	<i>AKARI</i>	0.45 (A)	19 μJy	Used
L15	15.23 μm	<i>AKARI</i>	0.42 (B)	31 μJy	Used
L24	22.75 μm	<i>AKARI</i>	0.42 (B)	78 μJy	Used
24 μm ^{c,e}	23.21 μm	MIPS	7.66	20 μJy ^e	Required
70 μm ^{c,e}	68.44 μm	MIPS	7.66	5.1 mJy ^e	Used
W1	3.353 μm	<i>WISE</i>	7.74	2.24 μJy	Not used (IRAC 3.6 μm instead)
W2	4.603 μm	<i>WISE</i>	7.74	4.58 μJy	Not used (IRAC 4.5 μm instead)
W3	11.56 μm	<i>WISE</i>	7.74	70.1 μJy	Used
W4	22.09 μm	<i>WISE</i>	7.74	530 μJy	Not used (MIPS 24 μm instead)
PSW (250 μm) ^{c,f}	242.8 μm	SPIRE	6.52	5.2 mJy	Required ^g
PMW (350 μm) ^{c,f}	340.9 μm	SPIRE	6.52	4.2 mJy	Required ^g
PLW (500 μm) ^{c,f}	482.3 μm	SPIRE	6.52	6.2 mJy	Required ^g

Notes.

^a From <http://svo2.cab.inta-csic.es/svo/theory/fps3/>.

^b The detection in at least two of these optical bands is required for a source in order to be considered in the analysis.

^c For additional information on how these data are extracted or included in the catalog, see Baronchelli et al. (2016a).

^d Original data from McMahon et al. (2013); Vista Hemisphere survey data release 2 expected depths.

^e Original data from Clements et al. (2011). The depths reported in Clements et al. (2011), 260 μJy and 2.4 mJy at 24 and 70 μm , respectively, correspond to the values where the 50% completeness is reached. Instead, the depths reported in this table correspond to the extrapolation at $S/N = 1$ of the flux vs. S/N ratio.

^f Original data from Oliver et al. (2012).

^g Only one detection at 250, 350, or 500 μm is required for a source in order to be considered in the analysis.

hereafter BA16). Besides the measures at 3.6 μm , the BA16 catalog includes observations at 4.5 (IRAC), 24 (MIPS), 250, 350, and 500 μm (*Herschel*/SPIRE), plus optical observations in the R_c band from the Wide Field Imager (WFI) of the European Southern Observatory/Max Planck Gesellschaft telescope (ESO/MPG). The 3.6 μm observations reach an average 3σ depth of 5.79 μJy at 3.6 μm (see Figure 1) and cover a total area of ~ 7 deg² (see Figure 2). Only 3.6 μm detected sources are included in this catalog.

In this work, we merged the BA16 catalog with a new set of UV, optical, and IR photometric measures. The resulting catalog now includes observations in 22 photometric bands (30 bands, considering observations taken by different instruments at similar wavelengths): far-UV, near-UV, *u*, *B*, *g*, *V*, R_c , *i*, *z*, *J*, *H*, *K_s*, 3.6, 4.5, 7, 11, 15, 24, 70, 250, 350, and 500 μm . This new photometric catalog is released through the NASA/IPAC Infrared Science Archive (IRSA), and it includes our best photometric redshift estimates, described in the following sections.

The complete list of bands, with the depth reached at each wavelength, is reported in Table 1. The depth is also represented for all of the bands in the catalog in Figure 1. In this figure, for each filter, we report the 3σ depths and the average flux of the faintest 1% percentiles of the sources included in the catalog. These values can be compared with the SED of a starburst galaxy (M82, from Polletta et al. 2007). The area covered in different bands is represented in Figure 2. Our analysis refers to the fraction of the optical area (green square in Figure 2) also covered by SPIRE observations (blue contour). We notice that this area is not fully covered by *AKARI* mid-IR observations. However, the same area is fully covered by *WISE* observations at ~ 11 μm .

As reported in Table 1, some of the filters (IRAC 3.6 μm , MIPS 24 μm , and one among the SPIRE bands) are “required,” meaning that all sources without a detection in one of these bands are excluded from our successive analysis. Other bands are simply “used” when available. Not all of the filters included in the catalog are required or even used for our analysis. Having a highly precise set of measures covering the whole SIMES field at 3.6, 4.5, and

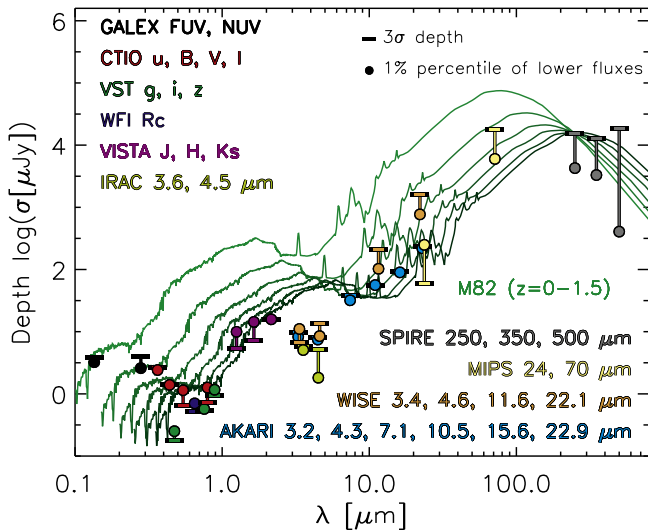


Figure 1. Depth (3σ) of the multiwavelength data in the SIMES field (horizontal thick lines). The faintest fluxes in the catalog (1% percentile) are also represented (filled circles). For comparison, the SED of the starbursting galaxy M82 (green line, from Polletta et al. (2007)) is shown for six different redshift values in the range $0 \leq z \leq 1.5$. The M82 SED is normalized to the $250 \mu\text{m} - 3\sigma$ depth.

$24 \mu\text{m}$ (IRAC and MIPS), we did not consider the lower-quality and redundant *AKARI* N3 and N4 (3.13 and $4.25 \mu\text{m}$, respectively) and *WISE* W1, W2, and W4 bands (3.35 , 4.60 , and $22.1 \mu\text{m}$, respectively). However, given the importance of the mid-IR spectral region when constraining the AGN emission, we considered the *AKARI* $24 \mu\text{m}$ band and both the *AKARI* and *WISE* $11 \mu\text{m}$ filters.

2.1. Mid-IR

2.1.1. WISE

The SIMES field is fully covered as a part of the *AllWISE* all-sky survey in the *WISE* W1, W2, W3, and W4 bands at 3.35 , 4.60 , 11.56 , and $22.09 \mu\text{m}$, respectively (Wright et al. 2010). The *WISE* survey scanning strategy resulted in frame-set depth of coverage that increased with increasing ecliptic latitude. Moreover, the sensitivity naturally improves toward the ecliptic poles due to lower zodiacal background. Therefore, in terms of depth, the SEP and northern ecliptic pole (NEP) are privileged fields. The SIMES field is located close to the SEP area.

Using the publicly available *AllWISE* tables describing the survey depth at different (R.A., decl.) coordinates,²² we estimated the average depths (1σ) in the SIMES area. They resulted in 2.24 , 4.58 , 70.1 , and $530 \mu\text{Jy}$ for W1, W2, W3, and W4, respectively.

At $11 \mu\text{m}$, the expected depth is of the same order of that measured for the *AKARI* S11 band ($19 \mu\text{Jy}$). While we limit the *AKARI* S11 catalog to only sources with S/N above the 3σ level, the *WISE* measurements in this band are reported down to the 1σ level, with a prior 5σ level detection in the W1 channel ($3.35 \mu\text{m}$) required. This guarantees a similar spatial density of sources measured in these two filters when a MIPS $24 \mu\text{m}$ detection is present, as we require in our analysis. Among the $24 \mu\text{m}$ sources detected in the *WISE-*AKARI** common area at all redshifts, 89% of the *AKARI* S11 detections have a measurement in the corresponding *WISE* filter. On the

other hand, 74% of the W3 measurements have a corresponding S11 detection. When limiting these data to the redshift range explored in our analysis ($0.15 < z < 0.3$), these fractions rise to 94% and 96%, respectively.

In our catalog, the IRAC $3.6 \mu\text{m}$ source associated with each *WISE* detection is the closest geometrical counterpart inside a $2''.68$ searching radius. This value corresponds to the square root of the sum of the variances of the IRAC $3.6 \mu\text{m}$ ($0''.705$) and *WISE* W1 ($2''.59$) point spread functions (PSFs).

2.1.2. AKARI/IRC

Between 3 and $24 \mu\text{m}$, the SIMES field is partially covered ($\sim 0.5 \text{ deg}^2$; see Table 1 and Figure 2) by *AKARI/IRC* observations (Onaka et al. 2007) in the N3, N4, S7, S11, L15, and L24 filters ($\lambda_{\text{ref}} = 3.13, 4.25, 6.95, 10.2, 15.2,$ and $22.8 \mu\text{m}$; PI: C. Pearson).

We computed the depth reached in each mosaic by measuring the flux inside randomly distributed apertures with diameter $\gtrsim 2 \times \text{FWHM}$ (see Table 2) and fitting a Gaussian function to the symmetrized distribution of the fluxes. In Table 1, we report the 1σ values of the fitted Gaussian functions.

We performed the source detection and extraction using the SExtractor software (Bertin & Arnouts 1996). In this phase, the coverage maps corresponding to each band are used as weight images. Following BA16, we considered total fluxes estimated in elliptical apertures with semimajor axis (a) proportional to the Kron radius (R_K ; Kron 1980) of each object (i.e., SExtractor “AUTO” fluxes). We considered only sources with five connected pixels above a threshold of 1σ of the local background. This choice guarantees that only $\sim 1\%$ of the sources included in the final catalog have fluxes lower than 3σ (see Figure 1).

For each *AKARI* band, the IRAC $3.6 \mu\text{m}$ counterpart is identified as the closest source found inside a search radius of $3''.73, 3''.73, 5''.20, 5''.66, 5''.68,$ and $6''.90$ for the bands N3, N4, S7, S11, L15, and L24, respectively. For N3 and N4, the searching radius corresponds to the quadratic sum of the PSF’s σ of the IRAC $3.6 \mu\text{m}$ and *AKARI* images. For the remaining *AKARI* bands, we found this choice too restrictive, given the overall quality of the *AKARI* final images. Combining the IRAC $3.6 \mu\text{m}$ and the *AKARI* PSF’s σ leads to the exclusion of an important fraction of real counterparts. In these cases, we found more reliable results using the *AKARI* FWHM (2.355σ).

2.2. Optical Data

The central square degree of the SIMES field (green square in Figure 2) is covered by ESO/WFI R_c (PI: T. Takeuchi; see BA16 for a detailed discussion) and VLT Survey Telescope (VST) $g, i,$ and z observations obtained as part of the INAF VST GT VOICE Survey Project (PIs: Covone & Vaccari; Vaccari et al. 2017). The VST mosaics were produced and calibrated at the VSTCen of the Osservatorio Astronomico di Capodimonte (INAF) using the VST-Tube pipeline (Grado et al. 2012, SAIT).

Half of this square degree ($\approx 64' \times 36'$) is covered by the Mosaic II camera²³ of the CTIO-Blanco telescope in the $u, B, V,$ and I filters (PI: C. Pearson). In Figure 2, this corresponds to the fraction of optical area below decl. $\approx -53^\circ 15'$. These CTIO data were reduced using standard IRAF routines included in the NOAO mosaic software MSCRED. All science frames were corrected by dividing them by the super-sky flat field (SSFF)

²² http://wise2.ipac.caltech.edu/docs/release/allwise/expsup/figures/sec2_3a_table2.tbl

²³ Retired in 2012 and replaced by the Dark Energy Camera (DECam).

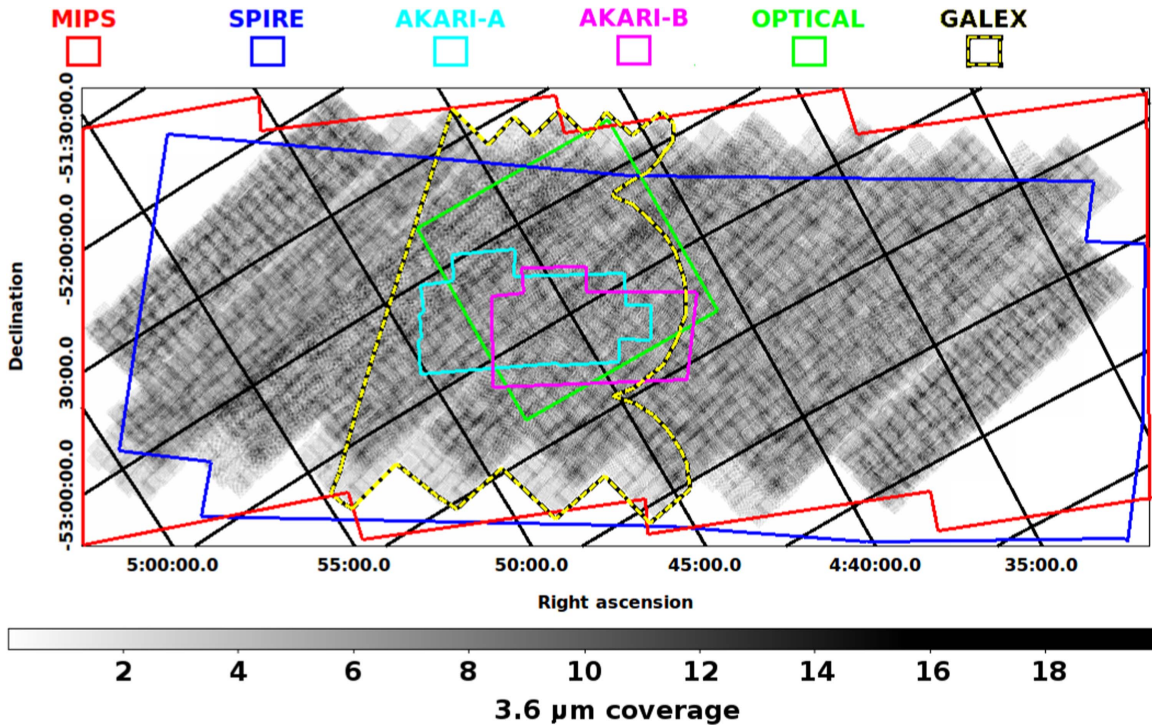


Figure 2. Coverage of the SIMES field by different instruments. The background image represents the coverage at $3.6 \mu\text{m}$ (*Spitzer*/IRAC). The coverage at $4.5 \mu\text{m}$ is similar, with a small shift ($\sim 6''$) toward lower declinations. The whole field is covered in the VISTA J , H , and K_s bands and by observations in the four *WISE* mid-IR bands ($3.3\text{--}22 \mu\text{m}$). Using different colors, we represent the coverage of *Spitzer*/MIPS (24 and $70 \mu\text{m}$, red), *Herschel*/SPIRE ($250\text{--}500 \mu\text{m}$, blue), *AKARI*-“A” ($3\text{--}11 \mu\text{m}$, cyan), *AKARI*-“B” (15 and $24 \mu\text{m}$, magenta), *GALEX* (black-and-yellow dashed), and optical bands (green). Our analysis (Section 6) focuses on the region covered by both optical and SPIRE observations. We notice that even if the important *AKARI* observations at 7 , 11 , and $15 \mu\text{m}$ do not cover the entire analysis area, this is sampled at $11 \mu\text{m}$ by *WISE* with a high detection rate among the SPIRE and MIPS detected sources ($\sim 94\%$) in the redshift explored ($0.15 < z < 0.3$).

image obtained by averaging all the nonaligned and source-subtracted science exposures in the same filter. The pixel scale and FWHM of the final mosaics are summarized in Table 3.

A precise photometric calibration of the optical mosaics is obtained through the comparison with Bruzual & Charlot (2003, hereafter BC03) template SEDs fitted to the optical data, as described in more detail in Section 2.5. As for the *AKARI* images, we calculated the depth of each optical image from the symmetrized distribution of the fluxes computed inside randomly distributed apertures with sizes $\gtrsim 2 \times \text{FWHM}$. In Table 1, we report the 1σ values of the Gaussian functions that better fit the symmetrized histograms.

For all of the bands listed above, the sources are detected and their fluxes measured using the SExtractor software, setting a minimum threshold of five connected pixels at the 1σ level above the local background for u , B , and R_c and 0.75σ for V , I , g , i , and z . This combination guarantees that only $\sim 1\%$ of the sources in the final catalog have fluxes lower than the estimated 3σ levels reported in Table 1 (see also Figure 1). The source extraction is weighted by considering the weight maps for the VST images and the rms maps for the CTIO mosaics.

The optical detections are included in the final catalog through two separate steps. First, we searched for possible counterparts in different optical bands inside a $1''0$ searching radius. In this particular case, we used the *matchn* function of the *stilts* software.²⁴ In a matched group, each detection is linked to a detection in another band; however, for any particular pair in a group, there is no guarantee that the two detections in two

Table 2
Main Properties of the *AKARI* Images^a

Parameter	<i>AKARI</i> Band					
	N3	N4	S7	S11	L15	L24
FWHM [arcsec]	4.23	4.23	5.15	5.62	5.64	6.86
Pixel scale [arcsec pixel ⁻¹]	1.46	1.46	2.34	2.34	2.45	2.45
1σ depth [μJy] ^b	3.2	2.7	13	19	31	78

Notes.

^a PI: C. Pearson.

^b Same values as in Table 1 and reported here for convenience.

different optical bands match each other, only that it is possible to pass from one to another through a series of pair matches. Only sources with detections in at least two different optical bands are included in the final catalog. In the second step, for each optical group, the IRAC $3.6 \mu\text{m}$ counterpart is identified inside a searching radius of $0''82$, corresponding to the quadratic sum of the σ of the IRAC $3.6 \mu\text{m}$ PSF and the searching radius used to create the optical catalog of sources ($1''0$).

We notice that even if only half of the central square degree is covered by all of the optical bands, this does not create selection biases: the u , B , V , and I bands, covering a smaller area, are shallower than the observations covering the whole square degree (see Figure 1).

2.3. VISTA J , H , and K_S

The SIMES field is fully covered by VISTA observations in the J and H bands and partially (78%) covered in the K_S filter as

²⁴ For more information, see <http://www.star.bris.ac.uk/~mbt/stilts/sun256/sun256.html>.

Table 3
Main Properties of the Optical Images

Parameter	Optical Band							
	u^a	B^a	V^a	I^a	R_c^b	g^c	i^c	z^c
FWHM [arcsec]	2.18	1.74	1.35	1.42	0.98	0.89	1.34	0.78
Pixel scale [arcsec pixel ⁻¹]	0.27	0.27	0.27	0.27	0.24	0.21	0.21	0.21
1σ depth [μ Jy] ^d	0.89	0.47	0.22	0.24	0.18	0.06	0.18	0.31

Notes.

^a CTIO-Mosaic II observations; PI: C. Pearson.

^b ESO/WFI observations; PI: T. Takeuchi. See Baronchelli et al. (2016a).

^c VST observations; PIs: G. Covone and M. Vaccari. See Vaccari et al. (2017).

^d Same values as in Table 1 and reported here for convenience.

part of the VISTA Hemisphere Survey (VHS; McMahon et al. 2013). These VISTA photometric measurements²⁵ are included in our multiwavelength catalog. We searched the $3.6\ \mu\text{m}$ -based catalog for the closest geometrical counterparts of the VISTA sources using a search radius of $0''.82$, corresponding to the quadratic sum of the IRAC $3.6\ \mu\text{m}$ PSF's σ and the approximate average seeing of the VISTA survey ($1''.0$) The J , H , and K_s measurements were finely calibrated using the technique described in Section 2.5.

2.4. GALEX

We included in our multiwavelength catalog a set of measurements obtained in the near- and far-UV (2274 and $1542\ \text{\AA}$) by the *GALEX* space telescope in the SIMES area (DR5). As in the other cases, we associated the $3.6\ \mu\text{m}$ sources with the geometrically closest *GALEX* counterpart using a $2''.2$ searching radius, corresponding to the quadratic sum of the IRAC $3.6\ \mu\text{m}$ and *GALEX* NUV PSF's σ . Only a fraction of the SIMES field is covered in the UV bands, and the average depth of the data (1σ) is $1.33\ \mu\text{Jy}$ in the NUV band and $1.27\ \mu\text{Jy}$ in the FUV channel. *GALEX* observations overlap well with the optical coverage. In Figure 2, the coverage is represented with a black-and-yellow line.

2.5. Refined Photometric Calibration

The photometric calibration of the bands from u to K_s is obtained in two separate steps. An initial calibration is obtained using different methods for different bands, while a subsequent refined calibration is obtained for all of the bands simultaneously using an iterative SED fitting technique.

For the VST g , i , and z bands, the initial calibration is obtained using the VST-Tube pipeline (Grado et al. 2012, M. Vaccari et al. 2018, in preparation), while for VISTA J , H , and K_s , we refer to McMahon et al. (2013). We computed the initial photometric calibration of the B , V , and R_c bands using the fluxes reported in the Zacharias et al. (2005) catalog of bright sources (including sources in the SIMES field) as a reference. For the u and I bands, we fitted the photometric data in all of the already-calibrated bands (through $4.5\ \mu\text{m}$) with stellar templates (Kurucz 1993). The reference fluxes that we use for the initial calibration of these two bands are those expected from the best-fitting stellar templates after the convolution with the filter responses.

²⁵ Second data release (DR2). For a detailed description, see https://www.eso.org/sci/observing/phase3/data_releases/vhs_dr2.pdf.

We refined these initial heterogeneous photometric calibrations through an iterative fit of galaxy SEDs (Bruzual & Charlot 2003) to a limited subset of high-quality data. In each iteration and for each band, we used the average difference between measured and expected fluxes (i.e., fluxes computed from the fitted SED) to correct to the calibration factors. For this process, we used only a subsample of ~ 150 sources with highly reliable fits ($\chi^2 < 1.0$) and known spectroscopic redshifts (Sedgwick et al. 2011) detected in four or more bands (excluding bands with $\lambda \geq \lambda_j$). The SED fitting procedure is performed using the *hyperz-mass* software (Bolzonella et al. 2000), a modified version of *hyperz* used to compute the best-fitting SED of sources of known redshift. We stopped the iterative process when both the average χ^2 and the calibration corrections were stable from one iteration to the following.

3. Photometric Redshifts

For the optically covered sources (green square in Figure 2), we computed photometric redshifts using all of the data available from the u band to $4.5\ \mu\text{m}$ (13 bands). The final redshift is the combination of the *hyperz* output (described in Section 3.1) with an optical prior (flux in the R_c , i , and z bands; see Section 3.2) that we considered only for $24\ \mu\text{m}$ detected sources. The use of the prior does not sensibly increase the average precision of the *hyperz* output, but, when tested on our high-quality spectroscopic sample (Sedgwick et al. 2011), after removing 10 probable quasars showing strong Mg II emission ($2798\ \text{\AA}$), it allows us to identify all the catastrophic outliers (i.e., $|\Delta z / (1 + z_{\text{spec}})| > 0.5$) and to supply a better redshift estimate in the majority of these cases. We tested the same method on a wider spectroscopic sample of COSMOS data using similar bands (Lilly et al. 2007; S. Lilly et al. 2017, in preparation). The final precision (dispersion in the $\Delta z / (1 + z_{\text{spec}})$ distribution) resulted in $\sigma_{\text{phot}} = 0.040 \pm 0.002$ for the SIMES data ($0.01 < z_{\text{spec}} < 0.9$; see Figure 6) and 0.048 ± 0.002 for the deeper COSMOS data ($0.01 < z_{\text{spec}} < 2.0$).

3.1. Redshift from SED Fitting

Using the *hyperz* software (Bolzonella et al. 2000), we fitted a set of BC03 templates to the total fluxes measured in the u , B , V , g , R_c , I , i , z , J , H , K_s , $3.6\ \mu\text{m}$, and $4.5\ \mu\text{m}$ bands. In the BC03 models, an exponentially declining SFR is assumed, with $\text{SFR} \propto \exp(-t/\tau)$, where $\tau = 0.3, 1, 2, 3, 5, 10, 15,$ and 30 Gyr. We consider a solar metallicity $Z = Z_{\odot}$ and an extinction law in the Calzetti et al. (2000) form, with A_V ranging from 0.0 to 4.0. The precision of this technique, when used alone, is tested using

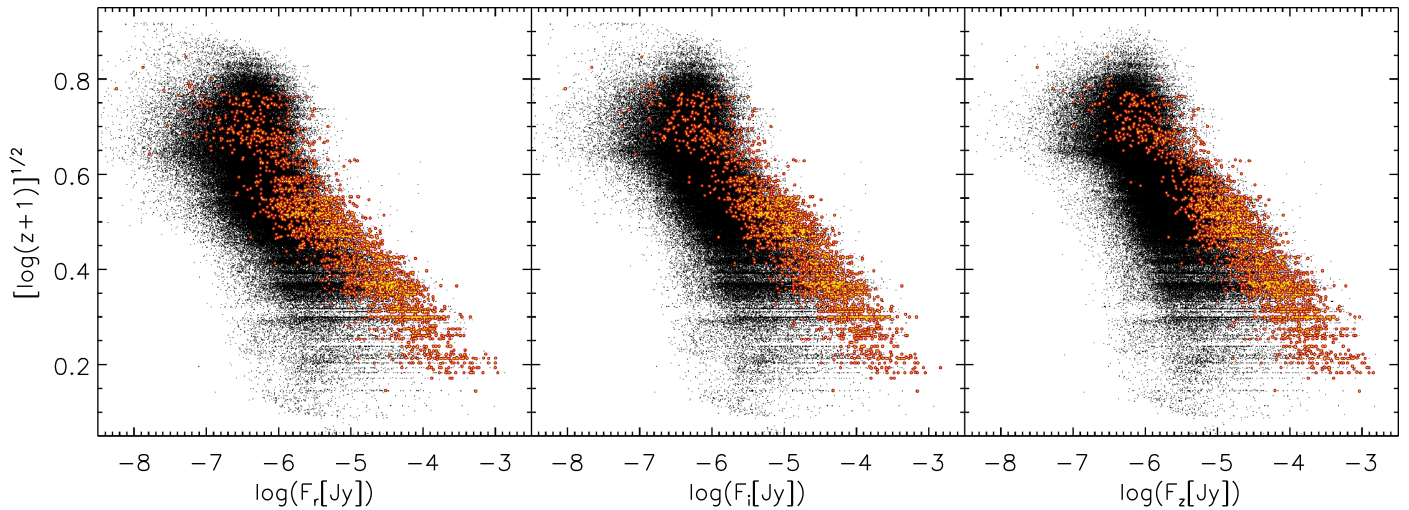


Figure 3. Observed optical flux vs. redshift relation for optical fluxes in the $r+$, $i+$, and $z+$ bands in the COSMOS field. Sources with $24\ \mu\text{m}$ fluxes $> 0.3\ \text{mJy}$ are highlighted in color.

the already mentioned SIMES and COSMOS spectroscopic samples. In the COSMOS field, in particular, we could perform an equivalent test using a similar set of photometric bands. We obtained a redshift precision $\sigma_{\text{Fit}} = 0.041 \pm 0.003$ in the SIMES field ($0.01 < z_{\text{spec}} < 0.9$; see Figure 6) and 0.046 ± 0.002 in the COSMOS field ($0.01 < z_{\text{spec}} < 2.0$). We notice that these uncertainties are computed from the Gaussian fit of the Δz distribution, excluding the catastrophic outliers (i.e., $|\Delta z / (1 + z_{\text{spec}})| > 0.5$). We identified six (4.2%) and 23 (6.7%) outliers in the SIMES and COSMOS spectroscopic samples, respectively.

3.2. Redshift from Optical Flux: A Complementary Technique

In order to improve the photometric redshift precision, we integrated the results of the SED fitting with the information given by the flux observed in three optical bands. The complementary technique described in this section, when combined with the χ^2 minimization results, allows the identification and correction of the outlier redshifts.

The simple idea at the basis of this method is that the more distant a galaxy is, the fainter it appears. Consequently, a broad inverse relation between optical fluxes and redshift is expected (see, e.g., Cowie et al. 1996). Here we demonstrate how the precision of this kind of relation is higher for far-IR selected sources. To this purpose, we studied the correlation between optical fluxes and photometric redshifts in the COSMOS field, where a large amount of data is available (Ilbert et al. 2010).

Figure 3 shows the optical flux measured in three optical bands (i.e., $r+$, $i+$, $z+$) versus $\sqrt{\log(z+1)}$. Sources with $24\ \mu\text{m}$ fluxes brighter than $0.3\ \text{mJy}$ are highlighted. The relation is evident even without a far-IR selection of the sources (black dots), but if the latter is considered, the same relation becomes narrower.²⁶

Starting from these observations, we computed the average ratios R_{rz} and R_{iz} between the fluxes measured in the $z+$ band, taken as reference, and those in the $r+$ and $i+$ bands,

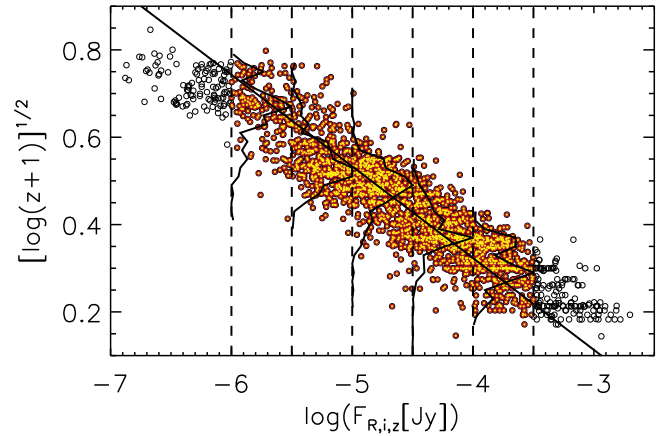


Figure 4. Combined optical flux $F_{r,i,z}$ vs. redshift relation (see Equation (1)) in the COSMOS field. Only $24\ \mu\text{m}$ detected sources ($F_{24} > 0.3\ \text{mJy}$) are considered here. We excluded the brightest ($F_{r,i,z} > 10^{-3.5}\ \text{Jy}$) and faintest ($F_{r,i,z} < 10^{-6}\ \text{Jy}$) sources (black circles) before computing the best linear fit.

respectively. Then we computed their quadratic sum as

$$F_{r,i,z} = \sqrt{\frac{F_z^2 + (R_{iz}F_i)^2 + (R_{rz}F_r)^2}{3}}. \quad (1)$$

Figure 4 shows the same relation between redshifts and optical fluxes presented in Figure 3 when the three optical bands are combined together in the $F_{r,i,z}$ measure. The best linear fit to these far-IR selected data, for $-6 < \log(F_{r,i,z}) < -3.5$, is

$$[\log(z_{\text{flux}} + 1)]^{1/2} = -0.51677 - 0.20997 \log(F_{r,i,z}). \quad (2)$$

In the same flux range, the average dispersion measured in five bins of flux is $\langle \sigma_{Vz} \rangle = 0.04$, with a maximum dispersion of 0.07 in the lowest flux bin.

After calibrating the flux–redshift relation using COSMOS photometric data, as explained above, we tested this method on a subsample of both COSMOS and SIMES spectroscopic data. For the SIMES field, we obtained $F_{r,i,z}$ from WFI R_c , VST- z_z , and i -band fluxes. Given the coefficients of Equation (2), the maximum acceptable $F_{r,i,z}$ is $3.46\ \text{mJy}$, since above this value

²⁶ We found similar results using PACS 100 and $160\ \mu\text{m}$ selections.

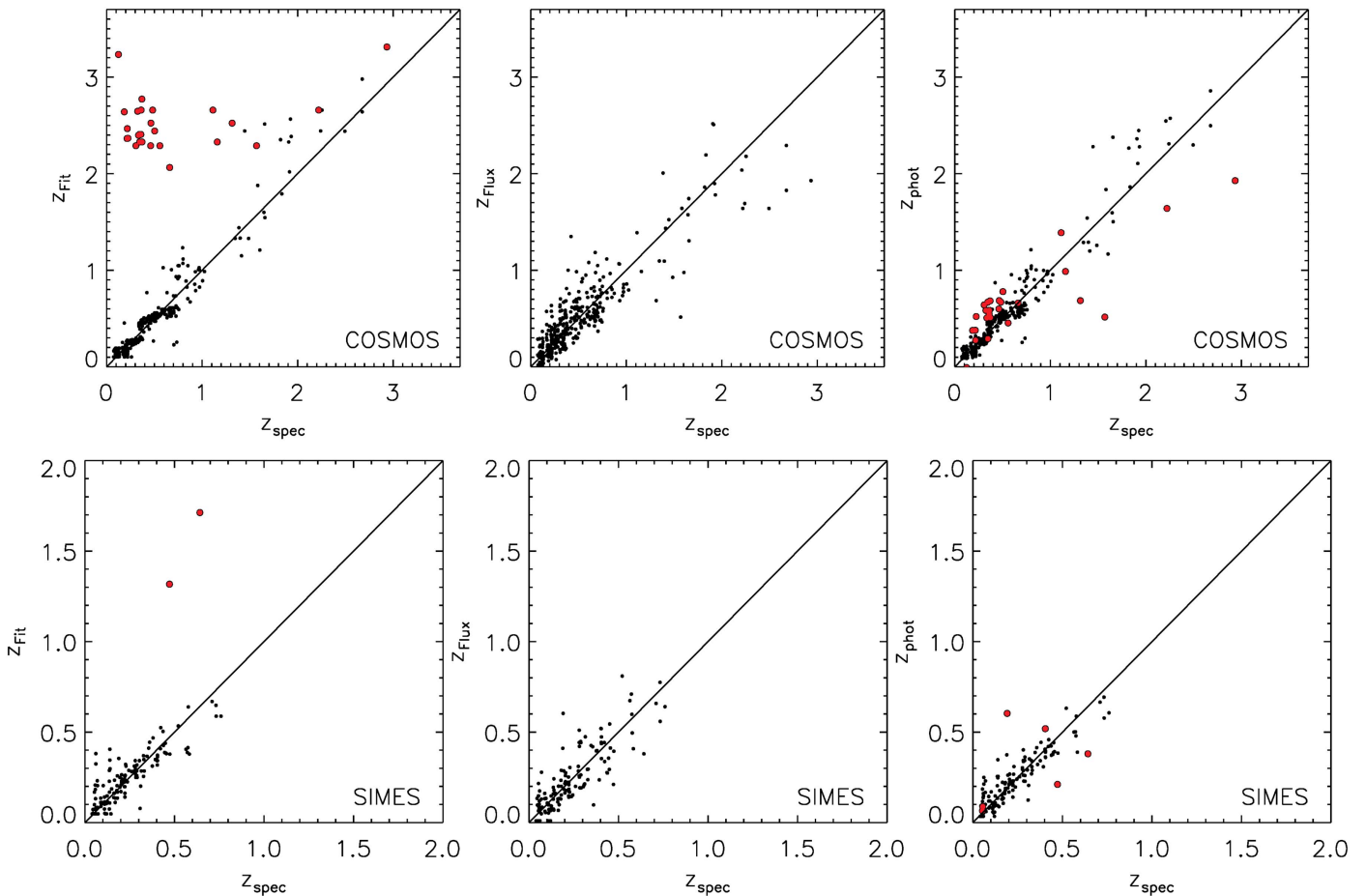


Figure 5. Spectroscopic and photometric redshifts in the COSMOS field (upper panels) and SIMES field (bottom panels). The comparison is shown between spectroscopic redshifts z_{spec} and *hyperz* outputs z_{Fit} (left panels), redshift obtained from optical fluxes z_{Flux} (central panels), and the combined technique z_{Phot} (right panels). The outliers affecting the SED fitting technique and identified through our method ($|z_{\text{Fit}} - z_{\text{Flux}}| > 1.0$) are represented with bigger red dots before (left panels) and after (right panels) the correction.

the resulting redshifts would be negative. In these rare cases, we set the redshift of the sources to $z_{\text{Flux}} = 0.01$.

If considered alone (i.e., not as a prior for the *hyperz* output), this flux-based method gives a redshift precision $\sigma_{\text{Flux}} = 0.093 \pm 0.007$ and 0.061 ± 0.004 in the COSMOS and SIMES fields, respectively. These precisions, as expected, are not higher than those resulting from the SED fitting technique. However, as can be observed in Figure 5, this method (z_{Flux}) is not sensitive to the catastrophic outliers problem affecting the SED fitting technique (z_{Fit}). We notice that the different Δz measured in COSMOS and SIMES does not depend on the different redshift distribution of the two spectroscopic samples (in the SIMES field, there are no spectroscopic redshifts above 1.0), and it does not substantially change when considering only sources at $z_{\text{spec}} < 1$ in both fields.

3.3. Combined Photometric Redshifts

We combined the redshifts resulting from the SED fitting technique (Section 3.1) and the observed optical flux (Section 3.2) using a weighted mean,

$$z_{\text{phot}} = W_{\text{Fit}} z_{\text{Fit}} + W_{\text{Flux}} z_{\text{Flux}}, \quad (3)$$

where the weights are given by

$$W_i = \frac{1/\sigma_i^2}{1/\sigma_{\text{Fit}}^2 + 1/\sigma_{\text{Flux}}^2} \quad \text{if } F_{24\mu\text{m}} > 0.3 \text{ mJy}$$

$$W_{\text{Fit}} = 1, \quad W_{\text{Flux}} = 0 \quad \text{if } F_{24\mu\text{m}} < 0.3 \text{ mJy}. \quad (4)$$

We fixed a threshold $|z_{\text{Fit}} - z_{\text{Flux}}| = 1.0$, above which $z_{\text{phot}} = z_{\text{Flux}}$. Using this threshold, we are able to identify a more precise solution (i.e., the same precision assigned to z_{Flux}) to the wrong outlier solutions resulting from the SED fitting strategy (see left and right panels of Figure 5).

Excluding the outliers, the precision of the *hyperz* output does not sensibly change when the optical prior is introduced (see Figure 6). However, all six and 23 outliers identified in the SIMES and COSMOS high-quality spectroscopic samples (corresponding to 4% and 7% of the total) can be corrected when using the combined technique described in this section (see Figure 5).

In Figure 7, we show the redshift distribution (z_{Fit} , z_{Flux} , and z_{Phot}) for all sources detected at $24 \mu\text{m}$ ($F_{24} > 0.3 \text{ mJy}$) in the SIMES field. Most of the outliers identified using the $|z_{\text{Fit}} - z_{\text{Flux}}| = 1.0$ threshold are distributed above $z_{\text{Fit}} \sim 1.7$, but this tail disappears in the z_{Phot} distribution after applying our correction technique.

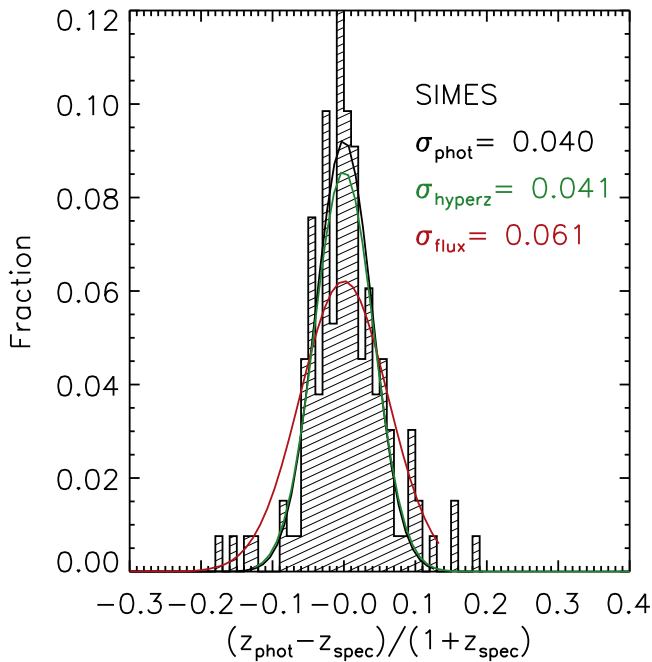


Figure 6. Redshift precision of the SIMES data. The histogram and its best-fitting Gaussian distribution (black line) refers to the results of the *hyperz* + prior technique that we used. The precisions of the *hyperz* output (green) and the optical prior (flux, red) considered separately are also reported for comparison.

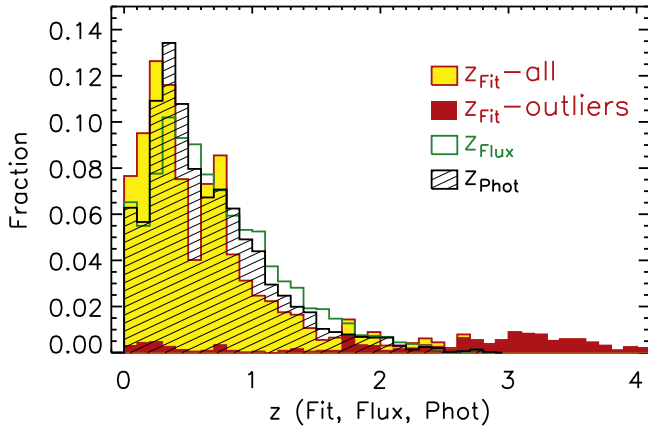


Figure 7. Redshift distribution in the SIMES field for $24\ \mu\text{m}$ detected sources ($F_{24} > 0.3\ \text{mJy}$) resulting from SED fitting (red and yellow), optical flux analysis (green), and combined technique (black). The red filled distribution represents the identified outliers before the correction.

3.4. Comparison with Different Software

We compared the technique described in Section 3.3 with a different algorithm, natively incorporating an optical prior. To this purpose, we computed the photometric redshifts for the SIMES spectroscopic sample (highest-quality only) using the *EAZY* software (Brammer et al. 2008). The SED fitting approach of *EAZY* is similar to that of *hyperz*, and it is based on the χ^2 minimization. Differently from *hyperz*, however, *EAZY* already incorporates the possibility of including a redshift prior based on the optical magnitude of the sources.

In our first experiment, we considered the *EAZY* prior based on the R magnitude of the sources. Therefore, we limited the test sample to sources detected in the R_c band. (This is not necessary using our method, where R , i , or z can also be used

separately). We obtained a number of outliers (four sources, corresponding to 3.6% of the sample) similar to what we find using *hyperz* without our prior. All four outliers are identified and corrected when using our method. Excluding these sources, the z precision is consistent between *EAZY* + internal prior and *hyperz* without prior ($\sigma_{\text{EAZY}} = 0.034 \pm 0.002$, $\sigma_{\text{hyperz}} = 0.038 \pm 0.003$).

In a second experiment, we considered the *EAZY* prior based on the K magnitude, comparing the results on a subset of K -detected sources. Again, the precision of the two methods is similar ($\sigma_{\text{EAZY}} = 0.032 \pm 0.003$ and $\sigma_{\text{hyperz}} = 0.036 \pm 0.003$), but *EAZY* is not able to identify five outliers that we are able to identify and correct using our method.

4. Galaxy Groups between $z \simeq 0.15$ and 0.3

In the central optically covered square degree of the SIMES field (green square in Figure 2), $\sim 66\%$ of the sources in the $3.6\ \mu\text{m}$ -based catalog of BA16 are detected in at least two bands among the U , B , V , R_c , I , g , i , and z . We used this sample of $\sim 38,000$ sources with a spectroscopic or photometric estimate of redshift to identify galaxy groups between $z \simeq 0.15$ and 0.3. At these redshifts, we could use a spectroscopic measure for $\sim 2\%$ of the sample and a photometric estimate, computed as described in Section 3.3, for an additional 9% of the sources with a far-IR measure of flux. For the remaining majority of the sources, for which a far-IR measure of flux is not available, the method described in Section 3.3 cannot be used. In these cases, we used the photometric redshift measure obtained using the *hyperz* software alone, as described in Section 3.1.

Having no data available at X-ray wavelengths, where clusters are often identified (e.g., Böhringer et al. 2004; George et al. 2011; Piffaretti et al. 2011), we find galaxy groups using an optically based friends-of-friends algorithm (Huchra & Geller 1982). This method is a simplified version of the approach described in Eke et al. (2004). We modeled the parameters of our group identification algorithm to find a compromise between the completeness of the group selection and the precision with which the sources in these groups are identified.

In our algorithm, for each galaxy, we search for possible surrounding group companions (“friends”) inside a comoving searching radius $\ell_{\perp} = 0.21(1+z)\text{Mpc}$. At high fluxes, the SIMES source number density is higher than that in the COSMOS catalog. To recreate the same SIMES $3.6\ \mu\text{m}$ flux distribution, we do not introduce simulated sources in the COSMOS data set. Instead, when a source brighter than $F_{3.6\ \mu\text{m}} \simeq 53\ \mu\text{Jy}$ is considered for a possible group membership, the linking radius connecting the source with another possible “friend” is allowed to be larger. In particular, since the average projected distance between sources depends on their numerical density as $d \propto n^{-1/2}$, the linking radius used for the test in the COSMOS field is set to

$$\ell_{\perp}(F_{3.6\ \mu\text{m}}) = 0.21(1+z) \min \left[\sqrt{\frac{n_{\text{SIMES}}(F_{3.6\ \mu\text{m}})}{n_{\text{COSMOS}}(F_{3.6\ \mu\text{m}})}}, 2 \right] \text{Mpc}. \quad (5)$$

As in Eke et al. (2004), we consider a cylindrical linking volume: for each source, the possible group companions are searched inside the radial interval $\Delta z = 1.5\sigma_z$, where σ_z is the photometric uncertainty of the source considered.

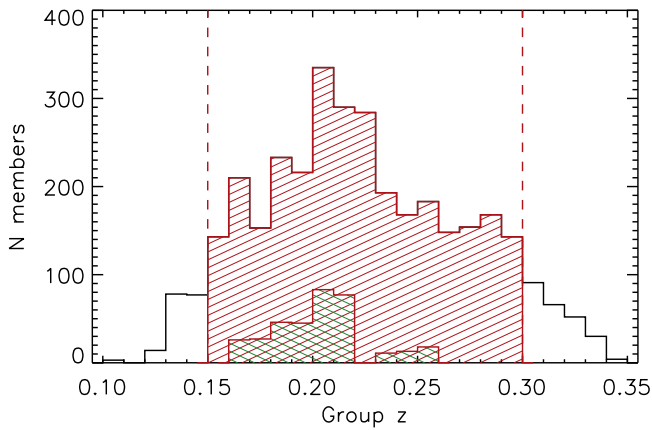


Figure 8. Redshift distribution of the groups found in the SIMES field. Groups with more than 10 member galaxies are highlighted in green. In the successive analysis, only groups with an average redshift $0.15 < z < 0.3$ are considered (red hatched area).

We tested our algorithm using COSMOS data (Ilbert et al. 2010), comparing our results with the COSMOS galaxy and X-ray group membership catalog described in George et al. (2011). In order to test our method on a data set as similar as possible to the SIMES data, in each $3.6 \mu\text{m}$ flux bin from the COSMOS catalog, we eliminated randomly distributed sources to reproduce the $3.6 \mu\text{m}$ flux distribution of the shallower SIMES catalog. We also added a noise component to the COSMOS photometric redshifts to simulate the same overall uncertainty measured in SIMES. The same test is run multiple times (100), each time creating a different data set, with statistically similar characteristics (however, the spatial distribution of the clusters and cluster members identified in the group membership catalog does remain original).

In the X-ray cluster catalog of George et al. (2011), only groups with more than 10 members are considered. Setting the same threshold in our test, we find an average of 450 ± 5 member galaxies in 19.8 ± 0.3 different groups in the redshift range $0.15 < z < 0.3$. $72\% \pm 1\%$ of the groups found in the different runs are identified as such in the George et al. (2011) group catalog, and $62.1\% \pm 0.4\%$ of the group members are reported in the reference catalog. The algorithm identifies $51.5\% \pm 0.5\%$ of the groups and $51.2\% \pm 0.6\%$ of the group members listed in the COSMOS X-ray.

Given an effective areal ratio $A_{\text{COSMOS}}/A_{\text{SIMES}} = 1.14$, using the same algorithm, 395 galaxies are expected to be members of 17.4 different groups with more than 10 sources in the SIMES area. In the SIMES field, we found 22 groups with more than 10 members, for a total of 346 sources. The Poissonian uncertainty on the number of groups identified in SIMES can justify the discrepancy with the expectation from the tests run in COSMOS. Instead, the different number of group members is the consequence of the presence of two particularly rich groups in the COSMOS area, both with more than ~ 50 sources and identified by the algorithm in each run, whereas no groups with so many members are present in the SIMES area in the same redshift interval. The presence of these two clusters justifies the difference in the number of total members identified. Figure 8 shows the redshift distribution of the groups. Groups with a minimum of two members are reported, and the richest groups with more than 10 components are highlighted. Figure 9 shows the (R.A., decl.) distribution of the same groups.

We found a total of 768 groups with at least two members. For each group, we estimate the total stellar mass M_{group}^* as the sum of the stellar masses of each single member identified. For each member galaxy, M^* is computed using the *hyperz-mass* software (Bolzonella et al. 2000). For the far-IR identified sources, we could estimate a more precise value of M^* using the multicomponent SED fitting approach described in Section 5.3. When possible, we used the more precise M^* estimates. However, given the extinction-dependent M^* difference between the two methods (see description in the same section for details), all of the *hyperz-mass* outputs are corrected as in Equation (7). Similarly to what was already done for the computation of the photometric redshifts with *hyperz* (see Section 3.1), we exploited all of the bands between CTIO *u* and IRAC $4.5 \mu\text{m}$. We considered a Calzetti et al. (2000) extinction law with A_V ranging from 0.0 to 3.0 (steps of 0.1). For the fit, we used a set of BC03 SSP models assuming $\text{SFR} \propto -t/\tau$, with $\tau = 0.3, 1, 2, 3, 5, 10, 15,$ and 30 Gyr.

5. Physical Properties of Far-IR Selected Galaxies

5.1. Sample Selection

In this work, we want to study the relations between BH and SF activity and relate them to the environmental properties of the host galaxies. To this purpose, we analyze the mid- and far-IR emission of AGNs and star-forming galaxies detected at the same wavelengths. Starting from the BA16 source catalog, based on $3.6 \mu\text{m}$ detections, we selected a sample of sources detected at $24 \mu\text{m}$ and in at least one of the 250, 350, or $500 \mu\text{m}$ SPIRE bands.

As for the study of the environmental properties at $0.15 < z < 0.3$, that we describe in Section 4; here we explore the optically covered area ($\sim 1 \text{ deg}^2$, represented by a green square in Figure 2). The optical coverage is a fundamental requirement to measure accurate photometric redshifts and stellar masses. For this reason, besides the $3.6 \mu\text{m}$ and far-IR selection, a detection is required in at least two optical bands among *U*, *B*, *V*, *R_c*, *I*, *g*, *i*, and *z*. Above $F_{3.6\mu\text{m}} = 100 \mu\text{Jy}$, roughly corresponding to the M^* limit that we adopt in the redshift range $0.15 < z < 0.3$ (see Figure 10), 87% have four or more detections in these bands. Of a total of 1262 far-IR detected sources, 883 (70%) respond to this requirement ($\sim 90\%$ above $F_{3.6\mu\text{m}} = 100 \mu\text{Jy}$). The completeness curve of the original BA16 sample is modified by the far-IR and optical selections, as described in Figure 10.

5.2. SED Fitting with SED3FIT

The optical-to-FIR SEDs of the galaxies in the selected sample have been analyzed using the three-component SED fitting code SED3FIT by Berta et al. (2013, hereafter BE13). Both photometric (see Section 3) and spectroscopic redshifts (Sedgwick et al. 2011), when available (112 sources below $z = 1.5$), were used. For the SED fitting, we used a maximum of 25 photometric bands between the far-UV and the far-IR: GALEX FUV and NUV; CTIO *u*, *B*, *V*, and *I*; WFI *R_c*; VST *g*, *i*, and *z*; VISTA *J*, *H*, and *K_s*; IRAC 3.6 and $4.5 \mu\text{m}$; AKARI 7, 11, 15, and $24 \mu\text{m}$; WISE 11 μm ; MIPS 24 and $70 \mu\text{m}$; and SPIRE 250, 350, and $500 \mu\text{m}$. In the mid-IR, the $11 \mu\text{m}$ band is covered by WISE and AKARI at the same time, while in the optical, we use both the CTIO *I* and the VST *i* observations. This reduces the number of not-redundant photometric bands to 23.

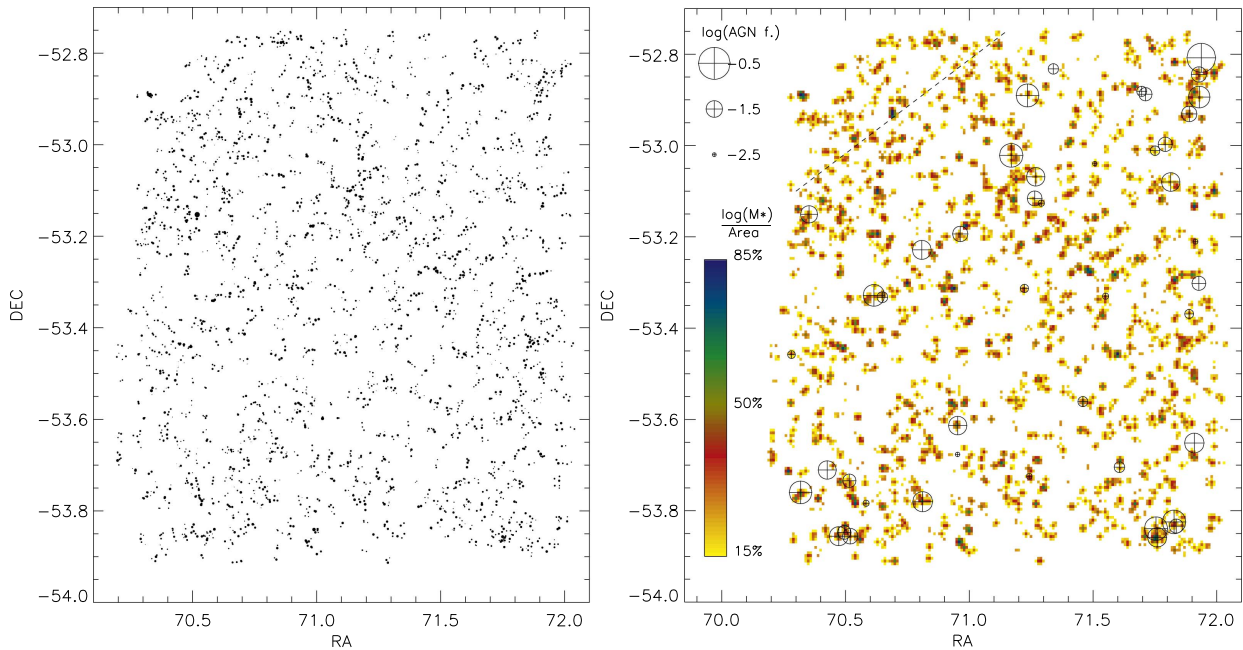


Figure 9. Left panel: spatial distribution of the groups identified in the SIMES field between $z = 0.15$ and 0.3 . Each point represents an actual galaxy member of a group, with bigger dots corresponding to higher stellar masses M^* . Right panel: stellar mass density of the groups in the same redshift bin. The color scale represents different fractions of the maximum value measured in the field. The AGNs identified are represented with circles proportional to the logarithmic bolometric AGN fraction. The diagonal dashed line represents the limit of the SPIRE coverage (no AGN analysis is performed above).

Originally inspired by da Cunha et al. (2008, hereafter DC08), SED3FIT computes the best-fitting SED as the combination of stellar emission, dust heated by the stellar population, and an AGN (torus+disk). Stellar and dust emission are linked by the energy balance between dust absorption in the optical spectral range and the reemission in the far-IR.

The adopted libraries of the models are stellar emission by BC03, using a Chabrier (2003) IMF and adopting a Charlot & Fall (2000) extinction curve; dust emission by DC08; and torus/AGN models by Fritz et al. (2006, 2016) in their latest implementation by Feltre et al. (2012).

The code produces the probability distribution function (PDF) for each single model parameter and relevant derived quantity (e.g., stellar mass, SFR, dust mass, $L(\text{IR})$). These PDFs are used to assess the degeneracy and uncertainty of each quantity.

Each torus model in the Feltre et al. (2012) library is identified by six different parameters: (1) ratio between the physical inner and outer radii ($R_{\text{out}}/R_{\text{in}}$), (2) opening angle, (3) $9.7 \mu\text{m}$ optical depth in the equatorial plane ($\tau_{9.7}$), (4) radial slope of the density profile (β), (5) height slope of the density profile (γ), and (6) inclination along the line of sight (θ).

Following Delvecchio et al. (2014), we limited the library to a subset of models covering a restricted range in parameter space (see Table 4). The $9.7 \mu\text{m}$ optical depth is limited to $\tau < 10$ (Pier & Krolik 1992), and $R_{\text{out}}/R_{\text{in}}$ ratios are restricted to values ≤ 100 , since no evidence is found for the existence of very extended torus geometries (Williamson et al. 2002; Tristram et al. 2007, 2009). As demonstrated in Delvecchio et al. (2014), the results obtained using the complete and the reduced libraries are consistent (see also Hatziminaoglou et al. 2008, 2009; Pozzi et al. 2012).

The unobscured bolometric AGN luminosity (L_{acc}), representing the unabsorbed total luminosity emitted by the nuclear object, is intrinsically associated with the best-fitting AGN model. Here L_{acc} accounts for the energy emitted by the central engine in the range 10^{-3} – $10^3 \mu\text{m}$, and it is simply related to the BHAR. The X-ray emission is considered negligible in the 8 – $1000 \mu\text{m}$ to L_{acc} conversion (4% of the total budget). This assumption relies on the large bolometric correction needed to convert X-ray emission to bolometric luminosity (20–30; Risaliti & Elvis 2004; Hopkins et al. 2007b; Pozzi et al. 2007; Vasudevan & Fabian 2009; Lusso et al. 2012).

After applying the SED fitting technique to the sources in our selection, we rejected 5% of clearly unreliable fits presenting a bad agreement between the photometric measures and the best-fitting SED. None of the rejected fits fall into the redshift range considered in our analysis (the majority of them are located between $z = 0.8$ and 2.0). In Figure 11, we show nine examples of fits obtained with the procedure described above.

5.3. Stellar Mass M^*

For each of the sources, the mass in stars M^* is derived from the PDF of the best-fitting BC03 models. In particular, we used the median of the PDF as an estimate of M^* .

As stated in Section 5.2, the SED fitting technique used accounts for possible emission from the central SMBH. Depending on the best-fitting AGN model, the SMBH emission can be responsible for a more or less important optical contribution. To assess the effects of the AGN on the estimated stellar masses, we compare the outputs of SED3FIT with those obtained using a SED fitting technique not involving any AGN component. For this comparative fit, we used all available

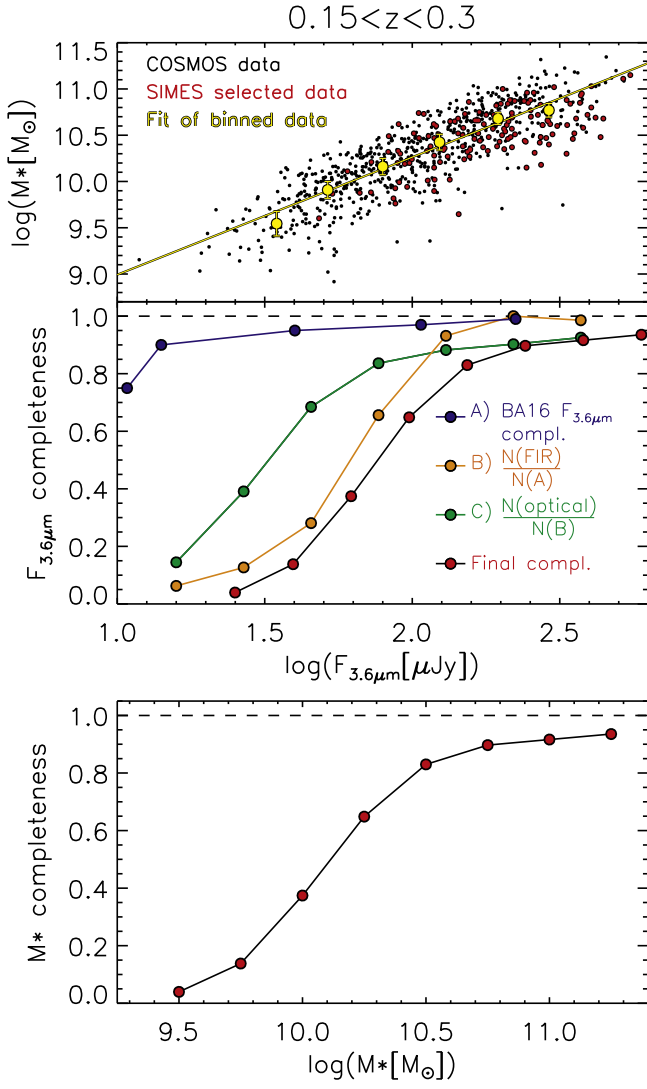


Figure 10. Upper panel: relation between $F_{3.6\mu\text{m}}$ and stellar mass M^* in the redshift interval $0.15 < z < 0.3$, as obtained using both SIMES data from BA16 and deeper COSMOS data from Rodighiero et al. (2011). All mass values are corrected as in Equation (7). Middle panel: final $F_{3.6\mu\text{m}}$ completeness function of our analysis sample (black curve, red dots) as a result of the combined effects of the different selections that we applied. From the initial catalog, for which the original $F_{3.6\mu\text{m}}$ completeness curve is computed in BA16 (blue), only far-IR detected sources (MIPS and SPIRE) are selected. This selection modifies the completeness of the original BA16 sample, as illustrated with the yellow line. Additionally, only optically identified sources are considered in the analysis. The effects of this selection are represented with a green line. Lower panel: mass completeness as a function of stellar mass M^* . This curve is obtained using the $F_{3.6\mu\text{m}}$ completeness function and the linear relation found between $\log(F_{3.6\mu\text{m}})$ and $\log(M^*)$.

bands between u and $4.5 \mu\text{m}$, the *hyperz-mass* software (Bolzonella et al. 2000), and the BC03 templates.

The comparison between the results of the two techniques is shown in Figure 12. In the same figure, the AGN fraction f_{AGN}^{λ} (i.e., the fraction of emission due to the SMBH) is shown for the 5–40 μm band.

Considering all of the data in our sample, we observe an average difference between the two methods:

$$\langle \Delta M^* \rangle = \left\langle \frac{M_{\text{SED3FIT}}^* - M_{\text{hyperzm}}^*}{M_{\text{hyperzm}}^*} \right\rangle \sim 0.6. \quad (6)$$

As can be observed in the central panel of Figure 12, this difference is not likely due to the introduction of the AGN component. The difference between the outputs does not depend in a significant way on the fraction of bolometric emission attributed to the SMBH. This is also expected when observing the typical AGN emission at the wavelengths where the stellar emission peaks (see Figure 11; note that the y axis is a logarithmic scale).

Instead, as found in Lo Faro et al. (2013), comparing *hyperz-mass*, *MAGPHYS* (da Cunha et al. 2008), and *GRASIL* (Silva et al. 1998; Vega et al. 2005) outputs, the difference arises particularly for luminous and ultra luminous infrared galaxies (LIRGs and ULIRGs) when trying to compute the stellar emission hidden by the dust. This difference is more prominent for heavily obscured sources (see left panel of Figure 12). Using a second-degree fitting curve, we found²⁷

$$\langle \Delta M^* \rangle = (0.534A_V^2 - 0.33A_V + 0.154) [M_{\odot}]. \quad (7)$$

Exploiting this extinction correction, we can combine the stellar masses computed using *MAGPHYS* or SED3FIT with the *hyperz-mass* results, as we do when estimating the stellar mass completeness of our sample (see Section 5.3.1). Given that *hyperz-mass* does not consider the far-IR emission to compute the extinction, whereas SED3FIT does, we use the results obtained with the latter as a reference.

5.3.1. Completeness Calculation

We estimated the stellar mass M^* completeness in the redshift range $0.15 < z < 0.3$ explored in our analysis. The completeness is computed by combining the 3.6 μm completeness function of the original sample, from Table 1 in Baronchelli et al. (2016a), and the linear relation between $\log(F_{3.6})$ and $\log(M^*)$ that we measured in the same redshift range using both SIMES and deeper COSMOS data from Rodighiero et al. (2011; see upper panel of Figure 10). Since the Rodighiero et al. (2011) stellar masses are computed using *hyperz-mass*, we corrected them according to Equation (7) to be consistent with our results, obtained with SED3FIT.

The data used in our analysis are a subsample of the 3.6 μm selected sample described in Baronchelli et al. (2016a). This subsample is selected following the criteria listed in Section 5.1. In the middle panel of Figure 10, we show how this series of selections affects the completeness as a function of the 3.6 μm observed flux. First, we compute how the far-IR selection (MIPS and SPIRE) affects the completeness of the reference BA16 3.6 μm selected sample (“All”). This curve is normalized to its maximum value. Then, we compute the completeness of the final sample with respect to the 3.6 μm and far-IR selected sample. The final combined 3.6 μm completeness function is obtained by multiplying these completeness curves. Using the linear relation between 3.6 μm fluxes and stellar masses (upper panel of Figure 10), we obtained the M^* completeness curve (lower panel of Figure 10).

5.4. Star Formation Rate

We computed the IR bolometric (8–1000 μm) luminosities (L_{FIR}) from the 50% percentiles of the PDFs resulting from the SED fitting technique. Following Kennicutt (1998,

²⁷ For this fit, we considered equivalent uncertainties along the y axis for all bins. This choice is made to give similar weight to differently populated bins of A_V .

Table 4
SED Fit Main Input Parameters

Parameter	Value	Description
Stellar models	BC03	...
IMF	Chabrier (2003)	...
Extinction law	Charlot & Fall (2000)	...
Dust emission	Three components	PAH + hot and cold components (star formation)
$R_{\text{out}}/R_{\text{in}}$	$10 \div 100$	Ratio between inner and outer radii of the dusty torus (AGN)
Θ	$40^\circ \div 140^\circ$	Dusty torus opening angle (AGN)
$\tau_{9.7}$	$0.1 \div 6$	Optical depth at $9.7 \mu\text{m}$
β	$-1 \div -0.5$	Radial slope of density profile (AGN)
γ	$0 \div 6$	Height slope of density profile (AGN)
θ	$0^\circ \div 90^\circ$	Torus inclination (AGN)

hereafter KE98), this quantity can be directly associated with the total SFR of a galaxy. The underlying KE98 assumption is that, for starbursting galaxies, the contribution of stars and AGNs to the total far-IR luminosity (8–1000 μm) is negligible when compared to the far-IR luminosity originating in the dusty star-forming regions. Using our SED fitting technique, we can separate the contributions to the total 8–1000 μm luminosity (L_{FIR}) due to stellar emission, AGNs (if present), and star-forming regions (i.e., $L_{\text{FIR}} = L_{\text{FIR}}^{\text{stars}} + L_{\text{FIR}}^{\text{SF}} + L_{\text{FIR}}^{\text{AGN}}$). We computed the SFRs of the sources using the KE98 equation but considering $L_{\text{FIR}}^{\text{SF}}$, instead of L_{FIR} , as an SFR tracer. The difference between L_{FIR} and $L_{\text{FIR}}^{\text{SF}}$ (and, correspondingly, the SFR computed) is higher than 25% in less than 5% of the cases (mostly extreme sources with $\log(\text{BHAR}/\text{SFR}) > -1.3$). Finally, since the original KE98 equation refers to a Salpeter (1955) IMF, we applied a 0.24 dex correction factor (e.g., Béthermin et al. 2013) to obtain the corresponding SFR values in a Chabrier (2003) IMF form.

Stellar masses and SFRs are expected to be related to each other by the so-called main sequence of the star-forming galaxies (Brinchmann et al. 2004; Elbaz et al. 2007; Noeske et al. 2007a; Rodighiero et al. 2011, 2014). We compared the SFR of each galaxy with the expectation resulting from the main-sequence definition of Elbaz et al. (2007; see Equation (4) therein), considering an SFR evolution as $(1+z)^{2.8}$ (Sargent et al. 2012). Again, we use the 0.24 dex correction factor to refer our quantities to a Chabrier (2003) IMF. The combination of the two equations can be expressed as

$$\text{SFR}_{\text{MS}}^{\text{Chab}}(z, M^*) = \frac{7.2}{1.7} (M^* \times 10^{-10})^{0.9} \left(\frac{1+z}{2} \right)^{2.8} [M_\odot \text{ yr}^{-1}]. \quad (8)$$

In Figure 13, we show the M^* versus SFR for three redshift bins in the redshift range $0.15 < z < 1.3$. The main sequence, computed for the average redshift of each bin by using Equation (8), is also shown for comparison. The almost-horizontal distribution of the data in the same plots is not surprising: given the far-IR selection of the sample (MIPS and SPIRE detections are required for our far-IR analysis), only the most IR-bright galaxies (i.e., the most star-forming) are considered at each redshift. However, this horizontal selection does not sensibly affect galaxies above the stellar mass completeness limit computed (for the redshift range explored in our analysis, see the vertical dashed line in Figure 13).

5.5. BHAR

The SED3FIT software provides the AGN bolometric luminosity (L_{acc}) as an output parameter. This luminosity, derived through SED fitting decomposition, is in good agreement with estimates obtained from X-rays and high-excitation mid-IR lines such as [Ne V] and [O IV] (Gruppioni et al. 2016). Following Mullaney et al. (2012), and assuming an energy production efficiency $\epsilon = 0.1$, we compute the BHAR of the sources in our selection as²⁸

$$\text{BHAR} = 1.586 \times 10^{-26} \frac{(1-\epsilon)L_{\text{acc}}}{\epsilon c^2} [M_\odot \text{ yr}^{-1}], \quad (9)$$

where c is in units of cm s^{-1} and L_{acc} is in units of erg s^{-1} .

The specific BHAR (sBHAR) is defined as the ratio between the BHAR and the BH mass M_{BH} . Using a simple conversion factor (e.g., Mullaney et al. 2012), the BH mass M_{BH} is obtained from the stellar mass of the host galaxy: $M_{\text{BH}} = 1.5 \times 10^{-3} M^*$.

5.6. Gas Fraction

For each of the sources in our sample, we computed the gas fraction from the total dust mass M_{dust} (a SED3FIT output) by combining the stellar mass–metallicity–redshift (M^* – Z – z) relation of Genzel et al. (2015; see Equation 12(a) therein),

$$\begin{aligned} \log(\text{O}/\text{H}) &= -12 + a - 0.087 [\log(M^* - b)^2], \quad \text{where} \\ a &= 8.74 \quad \text{and} \\ b &= 10.4 + 4.46 \log(1+z) \\ &\quad - 1.78 (\log(1+z))^2, \end{aligned} \quad (10)$$

with the δ_{GDR} – Z relation defined in Magdis et al. (2012),

$$\log \delta_{\text{GDR}} = 10.54 - 0.99 [12 + \log(\text{O}/\text{H})]. \quad (11)$$

Substituting the stellar mass M^* in the previous equations, the gas mass can be obtained from the total dust mass M_{dust} using

$$M_{\text{GAS}} = M_{\text{dust}} \delta_{\text{GDR}}. \quad (12)$$

5.7. AGN Fraction

Our analysis sample is made by low-redshift SPIRE-detected star-forming galaxies. Consequently, for all of the sources in the redshift range explored ($0.15 < z < 0.3$), the presence of an AGN has only marginal effects on the

²⁸ The bolometric luminosity L_{BOL} in Mullaney et al. (2012) corresponds to L_{acc} in this analysis.

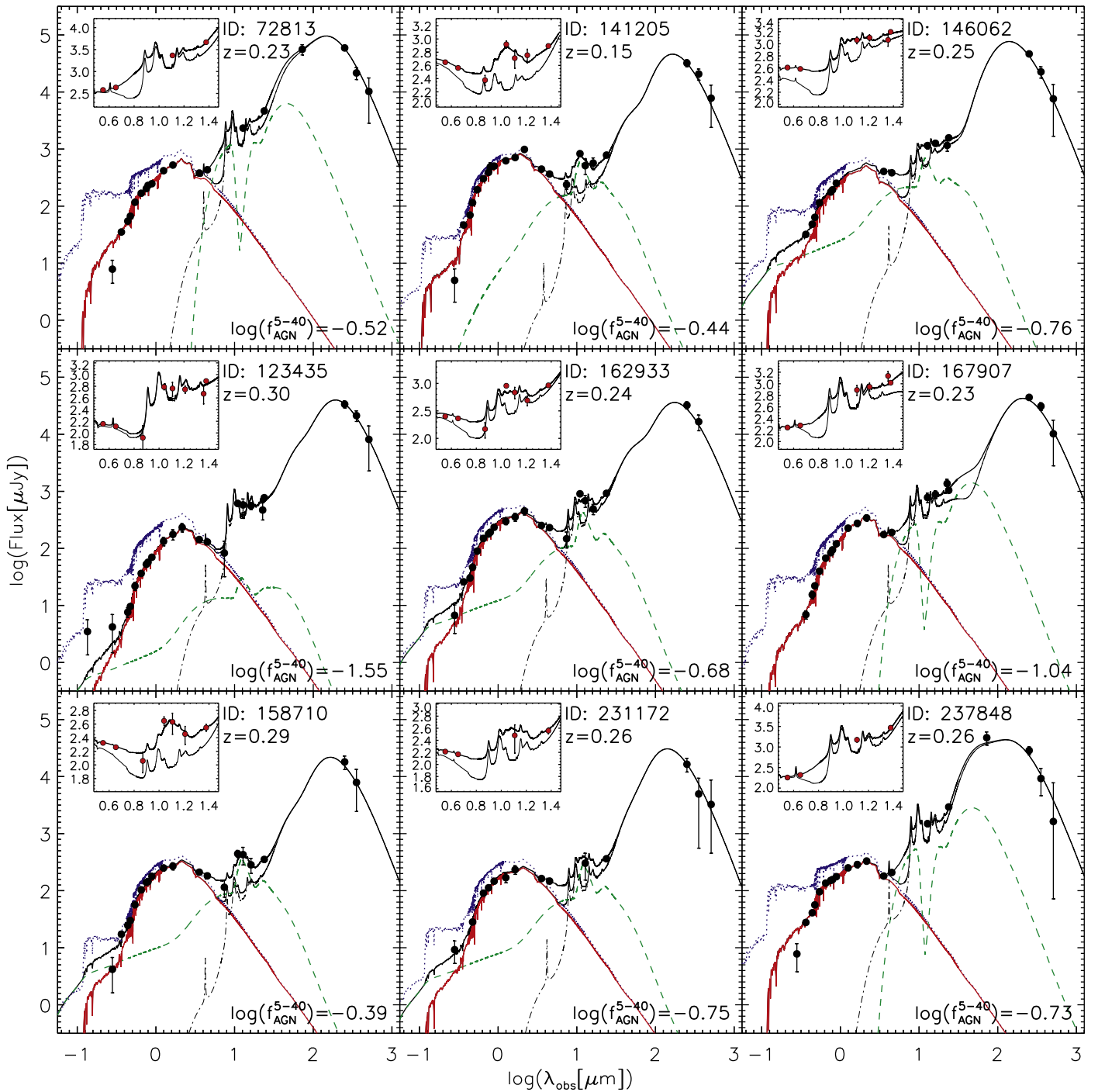


Figure 11. Examples of triple-component fits obtained using the SED3FIT software (Berta et al. 2013). The stellar emission is represented using solid red (observed) and dotted blue lines (unextincted), the AGN emission with a dashed green line, and the SF region emission with a dot-dashed black line. The thick solid black line is the sum of the three components (red, green, and dot-dashed black), while the thin solid black line represents the sum of stellar emission and SF only. The inserts represent the enlargement of the 3–30 μm spectral region. The lower, thinner line represents the best-fitting model if the AGN effects are not considered, while in the upper, thicker line, the dusty torus emission is considered.

computation of the total SFR. This can be visually appreciated by observing the typical SEDs represented in Figure 11: the total 8–1000 μm emission is always strongly dominated by the star formation. Consistently, we already showed in Figure 12 (middle panel) how the presence of an AGN does not affect the computation of the stellar masses in our sample. Similar results are found in Ciesla et al. (2015), where it is shown that including an AGN contribution in an SED fitting

has marginal effects on the computation of the total stellar mass of the galaxies, unless the AGN contribution itself dominates the IR emission.

In our analysis, we compute the AGN contribution to the IR luminosity in two different spectral ranges: 8–1000 μm (bolometric) and 5–40 μm . As demonstrated in Gruppioni et al. (2016), even when the AGN emission contribution to the bolometric band is small ($f_{\text{AGN}}^{8-1000} \sim 0.3\%$), the AGN

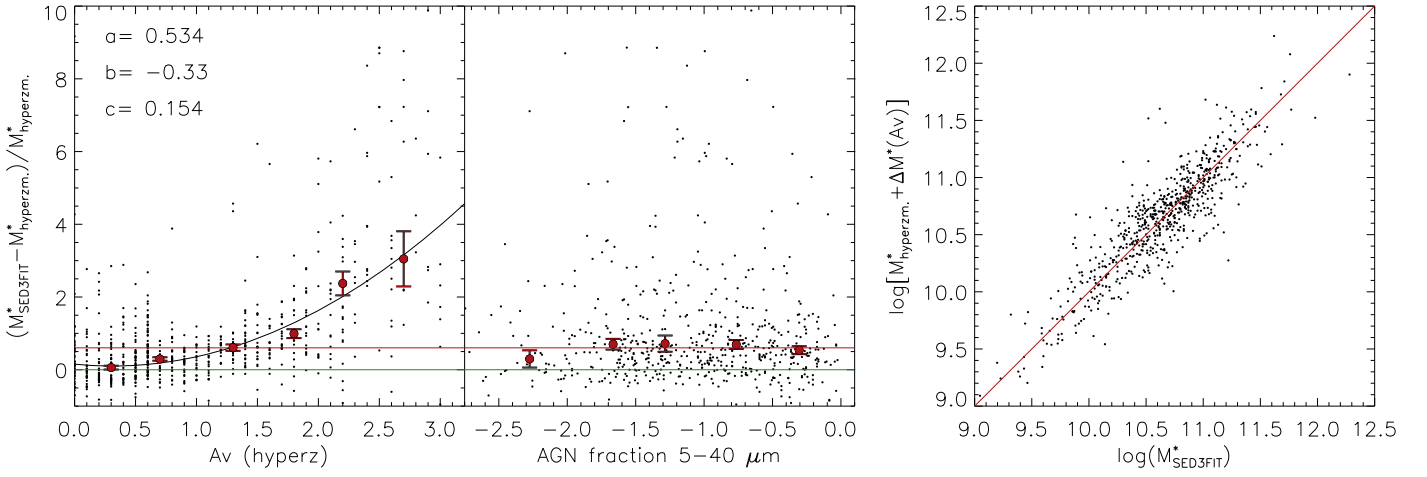


Figure 12. Comparison between stellar masses (in units of M_\odot) computed considering (SED3FIT) and not considering (*hyperz*) a possible AGN emission component. The green line represents the average value expected if the two methods did not produce any difference in the outputs (zero), while the red line is the average value measured. While there is no evidence for dependence on the AGN emission fraction between 5 and $40 \mu\text{m}$ (middle panel), there is a clear dependence on the extinction A_V (left panel). A similar result is found in Lo Faro et al. (2013) when comparing stellar masses computed using *hyperz* and *MAGPHYS* (da Cunha et al. 2008). In the right panel, we show the agreement between the stellar masses computed using the two methods after correcting the *hyperz*-mass results with the fit shown in the left panel.

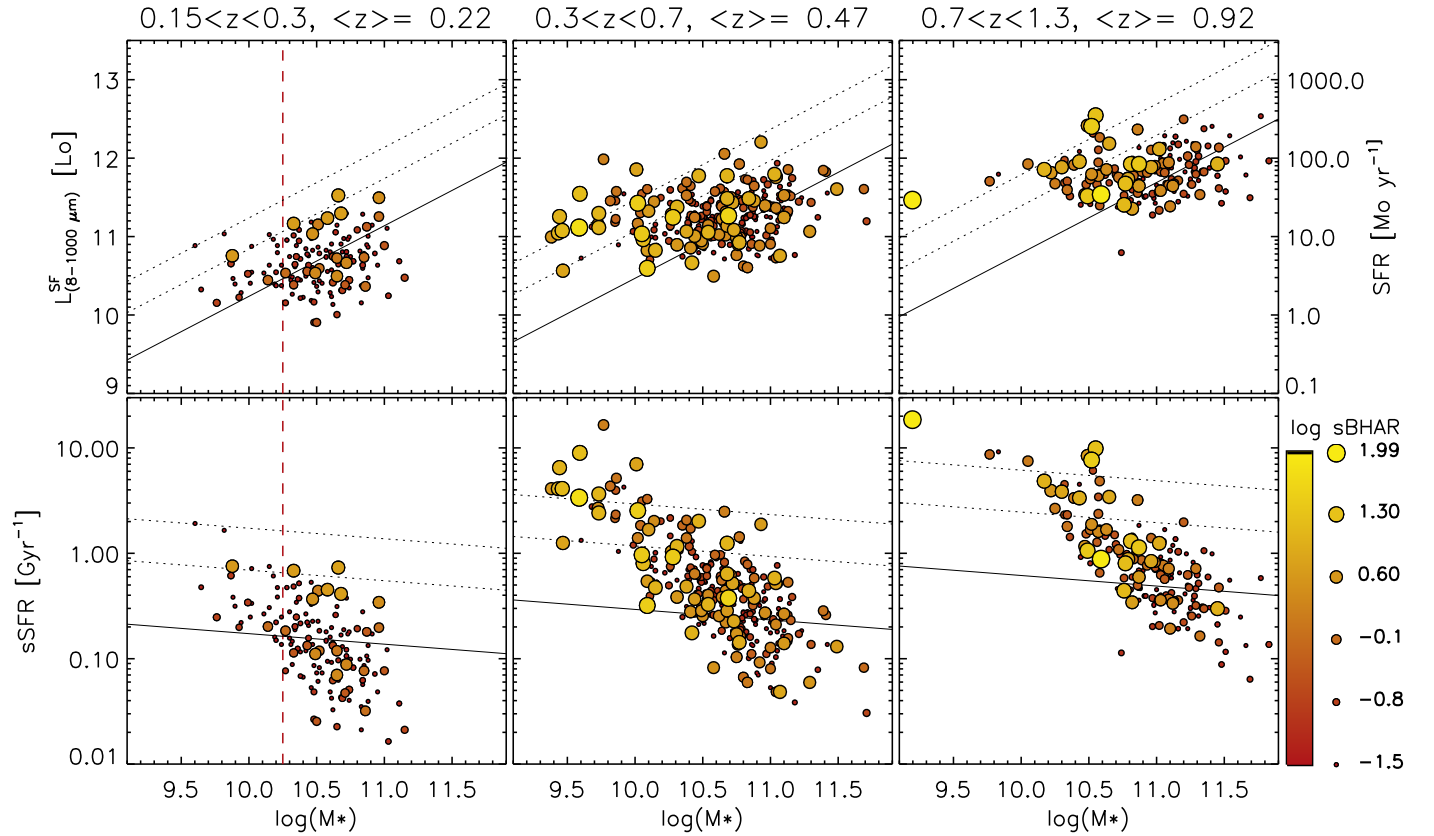


Figure 13. Upper panels: position of the data with respect to the stellar mass–SFR relation (black solid line computed using Equation (8) at the average redshift of the bin) in three redshift bins between $z = 0.15$ and 1.3 . Bigger circles and yellow color indicate higher sBHAR (Gyr^{-1}). The first redshift bin (left panels) corresponds to the redshift range explored in our analysis. The mass limit used in the analysis ($10^{10.25} M_\odot$) is indicated with a red dashed line. The black dotted lines indicate SFRs 4 and 10 times higher than the main-sequence value. The nearly horizontal distribution of the data, especially at higher redshifts, is expected: the sample is dominated by the far-IR selection (for example, see the distribution of a similar *Herschel*-selected sample in Rodighiero et al. 2011). In the lower panels, the distributions are shown in the M^* vs. sSFR plots.

contribution to the $5-40 \mu\text{m}$ (f_{AGN}^{5-40}) is around one order of magnitude higher and hence detectable if photometric measures are available in the rest-frame mid-IR spectral range (as in our case).

5.7.1. Uncertainties and Reliabilities

In Figure 14, we show the uncertainty related to $f_{\text{AGN}}^{\Delta\lambda}$ for all sources in the parent sample with an available fit. We observe

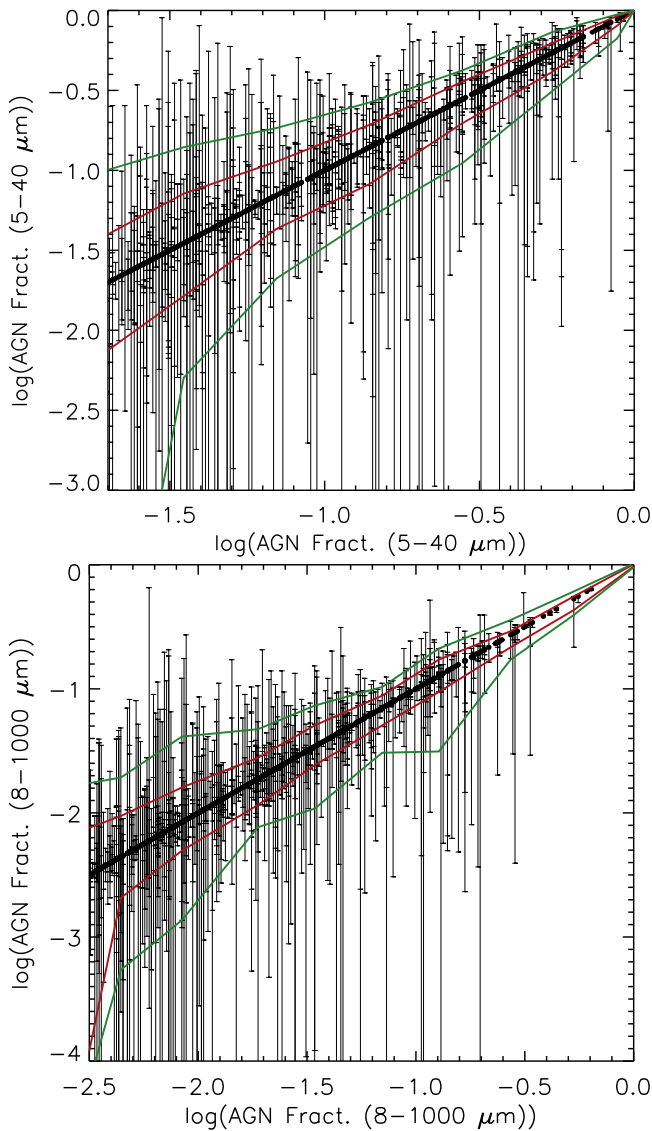


Figure 14. Uncertainty (1σ) associated with the fraction of IR emission due to AGNs. We consider two different bands: 5–40 μm (upper panel) and 8–1000 μm (bottom panel). Both axes represent the estimate of the AGN emission fraction for each galaxy. In the y axes, the upper and lower limits to these estimates are reported for each source. The red and green lines represent the median and 75% percentiles of the upper and lower limits after binning the data in the x axis.

that this uncertainty can be very high on some galaxies if considered singularly, but the median uncertainty (red line in Figure 14) is always smaller than ~ 0.3 in logarithmic scale, and for the vast majority of the sources (75%; green line in Figure 14), it is never larger than 0.5. We stress the fact that our analysis is based on the study of the average AGN emission fraction of binned data, while we are not using the fitted SEDs and the corresponding SED fitting-related parameters to get information at the level of single galaxies.

Finally, we notice that the average uncertainties explode below $f_{\text{AGN}}^{5-40} \sim 2\%$ or, equivalently, below $f_{\text{AGN}}^{8-1000} \sim 0.3\%$. Below these limits, it becomes statistically very difficult to distinguish between sources hosting low-activity AGNs and sources without AGN activity at all. This is also true after averaging the behavior of many sources. For this reason, we set this lower limit as a threshold: AGNs are considered in our analysis only when $f_{\text{AGN}}^{5-40} > 2\%$.

The previous one is not the only selection criterion applied: following Iyer & Gawiser (2017), we performed an additional F -test to select only the sources for which the AGN component statistically improved the SED fit, after considering the different number of degrees of freedom. To this purpose, we ran the *MAGPHYS* software (da Cunha et al. 2008; *MAGPHYS* does not natively include an AGN component) using a set of parameters similar to those used for our analysis, AGN component excluded. Given the number of photometric bands used in the fit (N_j), the χ^2 values obtained in the *MAGPHYS* (χ_1^2) and SED3FIT (χ_2^2) runs, and the different number of components used in the two cases ($N_1 = 2$ and $N_2 = 3$), we computed \mathcal{F} as

$$\mathcal{F}(\chi_{N_1}^2, \chi_{N_2}^2) = \frac{(\chi_{N_1}^2 - \chi_{N_2}^2)/(d_2 - d_1)}{\chi_{N_2}^2/d_2}. \quad (13)$$

In Equation (13), $d_1 = N_j - 3N_1$ and $d_2 = N_j - 3N_2$ represent the degrees of freedom corresponding to the number of components in the two runs. As in Iyer & Gawiser (2017), we rejected the additional AGN component when $p(\mathcal{F}, d_1, d_2) < 0.5$. The main results of our analysis are still valid without rejecting these fits, but in that case, the p -value of the relations that we find is an order of magnitude higher. Using the selection methods described, we identified an AGN component for $49\% \pm 7\%$ of our far-IR selected sample in the redshift range $0.15 < z < 0.3$.

Concluding, in our AGN sample, we included only the sources satisfying the following three criteria at the same time:

- the SED fitting software that we use (SED3FIT) finds an AGN emission component that improves the overall fit, following the χ^2 minimization method;
- the AGN contribution to the mid-IR emission, between 5 and 40 μm (f_{AGN}^{5-40}), is higher than 2%; and
- the AGN contribution is “statistically required” following the F -test described above.

5.7.2. Comparison with Diagnostic Methods

In this section, we compare the results of our AGN selection to two different diagnostic methods, based on mid- and far-IR photometric bands, that we designed following an approach similar to that proposed in Fadda & Rodighiero (2014). We found the combinations here proposed to be the most suitable for separating AGN-dominated systems from different types of galaxies. In our analysis, we study the galactic nucleus (SMBH) contribution to the total mid- and far-IR emission of a sample of star-forming galaxies. In this sense, we considered as AGNs only the sources satisfying the three criteria specified in Section 5.7.1. It is important to notice that with such a definition of AGN, we are not indicating “AGN-dominated systems” but rather “galaxies with a detected emission from the nucleus.” This difference is important when comparing our AGN sample to diagnostic methods such as the ones proposed here. In fact, these diagnostic methods are meant to detect AGN-dominated systems (i.e., AGNs showing a dominant contribution to the overall IR emission of the galaxies).

In the first of the two diagnostic plots that we propose (Figure 15), we combine the fluxes observed in the MIPS 24 μm and *AKARI* 15 and 7 μm bands with those measured at 3.6 and 4.5 μm (IRAC). On the x axis, we consider the IRAC

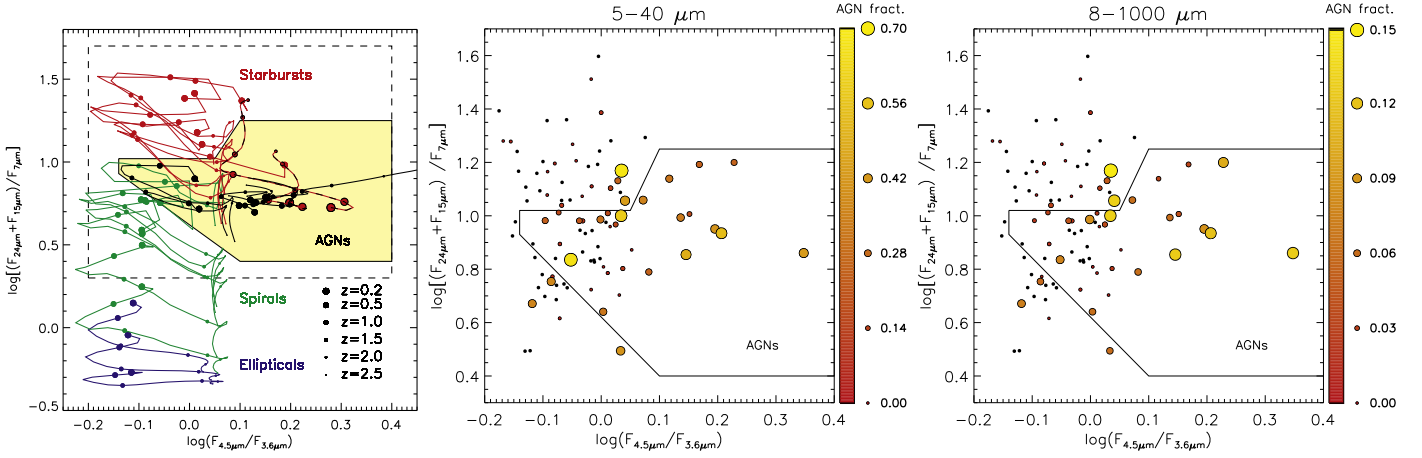


Figure 15. Position of our data (no redshift selection) with respect to the first of the two AGN diagnostic methods that we propose. In the left panel, we show the tracks traced by the Polletta et al. (2007) template SEDs in the first of the two diagnostic methods proposed by shifting the SEDs to different redshifts. Different types of galaxies are represented using different colors: ellipticals in blue, spirals in green, starbursts in red, and AGNs in black. Mixed types (AGN/starbursts) are represented with dashed red and black lines. The proper AGN area of the diagnostic plot (yellow shaded area) is drawn by trying to include the AGN templates avoiding the contamination from different templates as much as possible. In the middle and right panels, we show the position of the sources in our sample (no redshift selection). The dimension and color of the data points represent, for each source, the AGN fractional contribution to the 5–40 μm and bolometric (8–1000 μm) emission. We find that 58% of the AGNs of our sample are located inside the proper area of this diagnostic plot, with 29% contamination.

4.5 μm –to–3.6 μm flux ratio (as already done in, e.g., Donley et al. 2012, for similar purposes), while in the y axis, we use the mid-IR ratio $(F_{15\mu\text{m}} + F_{24\mu\text{m}})/F_{7\mu\text{m}}$ (a similar quantity is proposed in the diagnostic plots presented in Fadda & Rodighiero 2014). In the left plot of Figure 15, we show the tracks corresponding to all of the templates reported in the SWIRE library (Polletta et al. 2007), as observed at different redshifts. The templates are divided among ellipticals, spirals, AGNs, and starbursts. The same library also includes two templates referring to mixed-system starburst/AGNs. We define the “AGN area” of the diagnostic plot by observing the position of the corresponding (Polletta et al. 2007) templates. The area is delimited by the polygon defined by the following coordinates:

$$\begin{aligned} x &= [-0.14, -0.14, 0.1, 0.4, 0.4, 0.1, 0.05], \\ y &= [1.02, 0.93, 0.4, 0.4, 1.25, 1.25, 1.02]. \end{aligned} \quad (14)$$

The number of sources with an available measure in all these bands at the same time is mostly limited by the overlap between the areas covered by *AKARI* at different wavelengths. Their position in the diagnostic plot is shown in the middle and right panels of Figure 15. We found that 58% of the sources identified as AGNs at all redshifts are included in the proper AGN area of this diagnostic plot, with 29% contamination from the other sources of our far-IR selected sample.

In the second diagnostic plot that we propose (Figure 16), we combine the IRAC 4.5 μm –to–3.6 μm flux ratio with the SPIRE 250 μm –to–*WISE* 11 μm ratio in a unique indicator. Then, the y axis is represented by $(F_{250\mu\text{m}}/F_{11\mu\text{m}}) \times (F_{3.6\mu\text{m}}/F_{4.5\mu\text{m}})$. In this quantity, at least for galaxies at $z \leq 1.5$, $(F_{250\mu\text{m}}/F_{11\mu\text{m}})$ represents an estimate of the relative AGN emission contribution with respect to the total far-IR emission (i.e., SFR). At the same time, the $(F_{4.5\mu\text{m}}/F_{3.6\mu\text{m}})$ ratio is a measure of the relative contribution of the AGN emission with respect to the total stellar emission (this is valid, at least, for the low redshifts explored in our analysis). The x axis of the diagnostic plot, $(F_{24\mu\text{m}}/F_{4.5\mu\text{m}})$, is mostly a measure of sSFR (SFR/M^*), but given the mid-IR nature of the two bands involved, it is also influenced by the AGN

contribution. In this second case, the AGN area of the diagnostic plot is delimited by the polygon defined by the following coordinates:

$$\begin{aligned} x &= [0.2, 0.55, 0.55, 1.9, 1.2, 0.6, 0.2], \\ y &= [2.15, 1.2, 0.3, 0.3, 1.7, 2.05, 2.15]. \end{aligned} \quad (15)$$

Using this diagnostic method, 63% of the AGNs identified are located in the corresponding AGN area of the plot, with 43% contamination.

6. Discussion

6.1. SMBH Activity in Small Groups

We studied the dependence of the AGN activity on the total stellar mass M_{group}^* of the hosting groups in the redshift interval $0.15 < z < 0.3$. For this analysis, we considered main-sequence galaxies ($-0.6 < \log(\text{SFR}/\text{SFR}(\text{MS})) < 0.6$) for which the SED3FIT software identified an AGN contribution to the total IR luminosity $f_{\text{AGN}}^{5-40} > 2\%$. Following Iyer & Gawiser (2017), we additionally performed an *F*-test to select only the sources for which the AGN component statistically improved the SED fit at the net of the different number of degrees of freedom (see Section 5.7.1).

In order to create a mass-complete sample, we exclude from our analysis AGNs in galaxies with $\log(M^*) < 10.25 M_{\odot}$. However, the total stellar mass of the groups, M_{group}^* , is computed using all of the galaxies identified as members, without exclusions.

We divided the sample into 10 “field” AGNs, for which the group finder algorithm did not find any companion (all of these sources have a *WISE* 11 μm flux measure, and one has a spectroscopic redshift), and 35 “group” AGNs with at least an identified companion (33 with an 11 μm flux measure, four with a spectroscopic redshift). The AGNs in groups are further divided into three bins of M_{group}^* .

Figure 17 shows the BHAR of single galaxies as a function of the total stellar mass of the hosting groups M_{group}^* . We see that BHAR increases with M_{group}^* , indicating that, on average, more massive groups host more accretion onto SMBHs. We

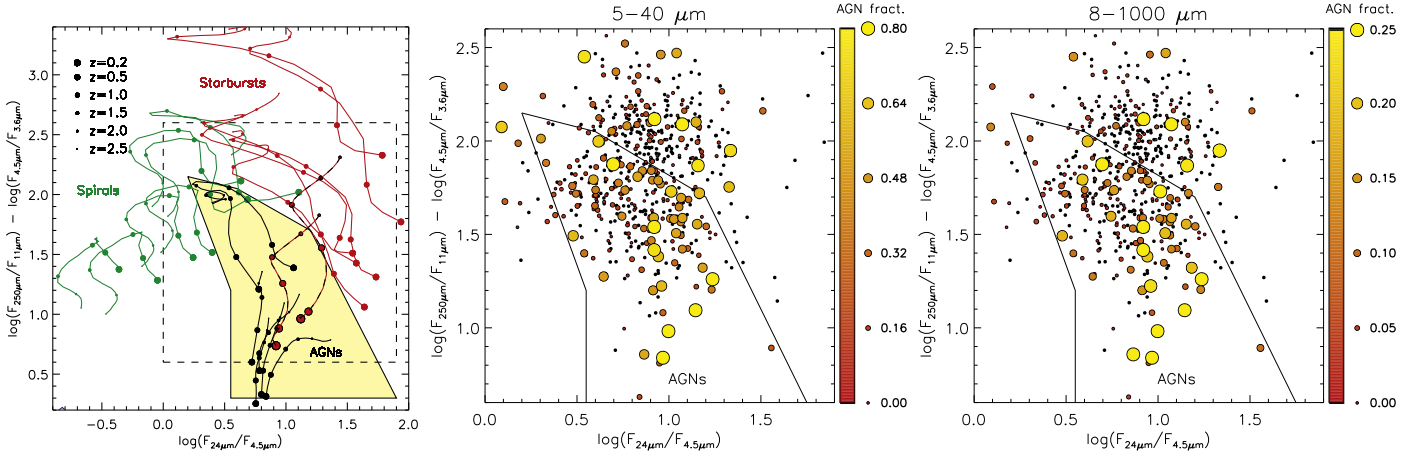


Figure 16. Position of our data (no redshift selection) with respect to the second of the two AGN diagnostic methods that we propose; colors and symbols are the same as in Figure 15. In this case, 63% of the AGNs of our sample are located inside the proper area of this diagnostic plot, with 43% contamination.

found $\log(\text{BHAR}) \propto (1.21 \pm 0.27)\log(M_{\text{group}}^*)$, with a correlation index $R = 0.61$ and a corresponding p -value equal to 0.010%. In order to facilitate the comparison with literature studies based on X-ray data, in the same figure, we indicate the BHAR values corresponding to some commonly used X-ray luminosity thresholds. These BHAR thresholds are obtained using Equation (9) and considering a conversion factor $L_{\text{acc}} = 22.4L_X$ as in Mullaney et al. (2012).

In Figure 18, we show how various AGN properties correlate with M_{group}^* . We see a moderate direct correlation between the AGN emission fraction computed for each galaxy in the bolometric (8–1000 μm) and 5–40 μm bands and the total stellar mass of the hosting group. In particular, we find $\log(f_{\text{AGN}}^{5-40}) \propto (0.57 \pm 0.14)\log(M_{\text{group}}^*)$ and $\log(f_{\text{AGN}}^{8-1000}) \propto (0.76 \pm 0.15)\log(M_{\text{group}}^*)$. The AGN emission fraction in these two wide far-IR bands is closely related to the ratio between the thermal emission of the dusty circumnuclear torus and molecular clouds in star-forming regions. For the BHAR/SFR, we find $\log(\text{BHAR}/\text{SFR}) \propto (1.04 \pm 0.24)\log(M_{\text{group}}^*)$. The correlation coefficient R of the linear fits to the data is higher than 0.58 in all three cases, while the corresponding p -values are lower than 0.023%.

On average, the BHAR, BHAR/SFR ratio, and AGN fraction, as well as their dispersions, are similar in the field and group galaxies, if the group galaxies are not divided in bins of M_{group}^* . However, the same quantities are generally higher among field galaxies than in groups, when $M_{\text{group}}^* \sim \langle M_{\text{field}}^* \rangle$.

The correlation that we identify can be explained as an sSFR decreasing with M_{group}^* and/or an increasing sBHAR. From the first two panels of Figure 19, the second of the two possibilities seems to be the most likely. While the sSFR does not seem to depend on the total stellar mass of the group, the sBHAR increases at higher values of M_{group}^* .

Following Gisler (1978), Dressler et al. (1985, 1999), Hill & Oegerle (1993), Kauffmann et al. (2004), Rines et al. (2005), and Popesso & Biviano (2006), the numerical fraction of AGNs in the field (f_{field}) is expected to be higher than in clusters (f_{group}). However, as suggested by various works (Coziol et al. 2000, 2004; Turner et al. 2001; Tovmassian et al. 2006), the AGN activity seems to be higher (or at least consistent) in small compact groups than in the field. While in the papers mentioned above, AGNs are identified using their X-ray emission, in this work, AGNs are selected using the fraction of

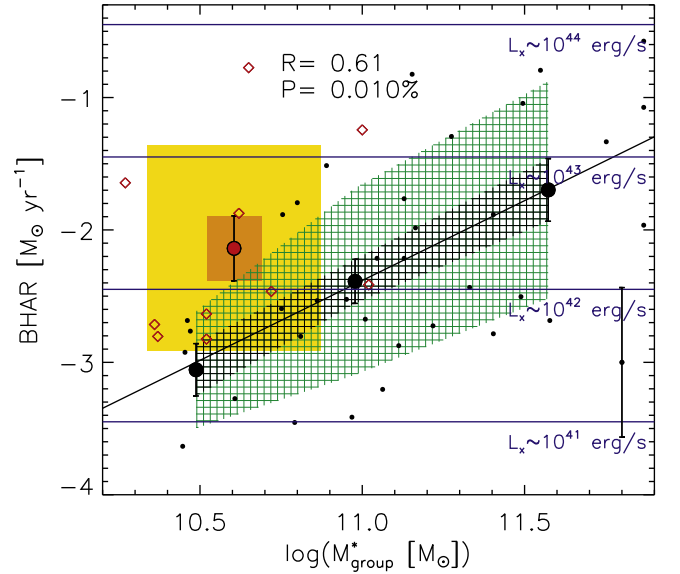


Figure 17. BHAR of galaxies in the field (red diamonds) and groups (black circles) as a function of stellar mass. For field galaxies, the x axis represents the stellar mass M^* of each single galaxy, while for galaxies in groups, it represents the total stellar mass of the hosting group (M_{group}^*). We considered three bins of $M_{\text{group}}^* - M_{\text{group}}^*[M_{\odot}] < 10^{10.75}$, $10^{10.75} < M_{\text{group}}^*[M_{\odot}] < 10^{11.25}$, and $M_{\text{group}}^*[M_{\odot}] > 10^{11.25}$ —but the linear fit is computed on the underlying data points, not on the binned data (only galaxies in groups are considered for the fit). The vertical dispersion in the three bins is shown as a hatched green area, while the batched black area corresponds to the 1σ uncertainty associated with the average values of BHAR in each mass bin. Dispersion and 1σ uncertainties are also represented for field galaxies using different tonalities of yellow. The typical uncertainty associated with each single data point is reported in the bottom right corner of the plot; its value is derived from the estimated PDFs of L_{acc} (see Equation (9)); that is, an output parameter of the SED fitting. The correlation coefficient R and the corresponding p -value are reported. For an easier comparison with literature results, the BHAR values corresponding to four X-ray-luminosity values are represented by horizontal blue lines.

IR emission due to the BH accretion as a discriminant. As described in Section 5.2, this emission fraction can be estimated only when a far-IR detection (MIPS and SPIRE) is available (i.e., mostly for late-type star-forming galaxies). Consequently, we can only compute the numerical fraction of AGNs among far-IR detected star-forming galaxies in the field ($f_{\text{field}}^{\text{IR}}$) and in groups ($f_{\text{group}}^{\text{IR}}$). For this reason, these values cannot be directly compared with the results of the works

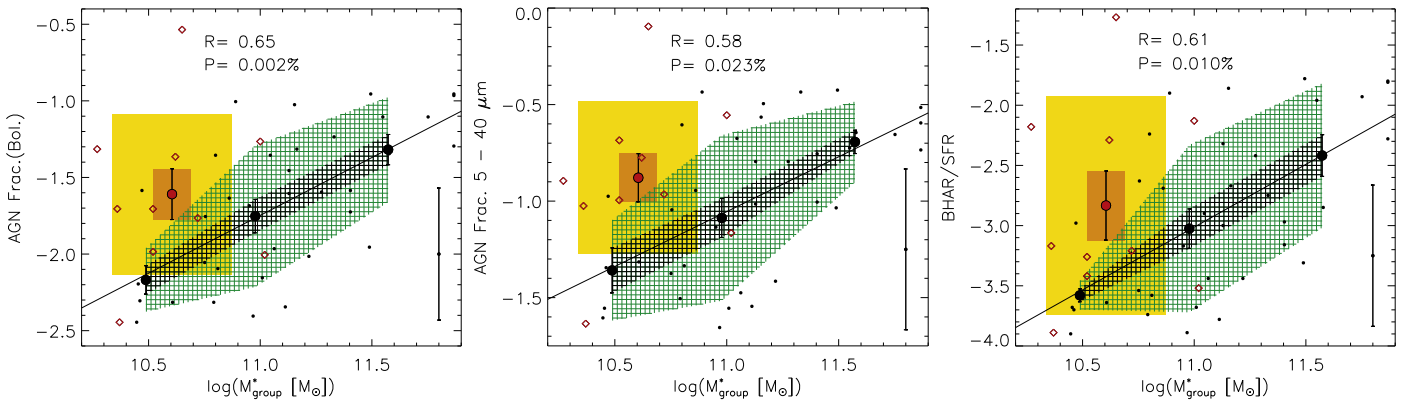


Figure 18. Left and middle panels: AGN fractional contribution to the total luminosity in the bolometric (8–1000 μm) and 5–40 μm bands as a function of the total stellar mass of the hosting galaxy group, M_{group}^* , at $0.15 < z < 0.3$. For field galaxies (red squares), the x axis represents the stellar mass M^* of each single galaxy, while for galaxies in groups (black circles), it represents the total stellar mass of the hosting group (M_{group}^*). We considered three bins of M_{group}^* — $M_{\text{group}}^* [M_{\odot}] < 10^{10.75}$, $10^{10.75} < M_{\text{group}}^* [M_{\odot}] < 10^{11.25}$, and $M_{\text{group}}^* [M_{\odot}] > 10^{11.25}$ —but the linear fit (solid line) is computed on the underlying data points, not on the binned data (only galaxies in groups are considered for the fit). The vertical dispersion of the data in the three bins of M_{group}^* is represented with a hatched green area, while the darker area corresponds to the σ . The yellow and orange areas represent the dispersion and σ of field galaxies. The typical uncertainty associated with single data points is reported in the bottom right corner of each plot. These uncertainties are derived from the estimated PDFs of each output parameter of the SED fitting that is required to compute the quantity in the y axis. The correlation coefficient R of the linear fit and the corresponding p -value are reported. Right panel: BHAR/SFR as a function of M_{group}^* for the same sources.

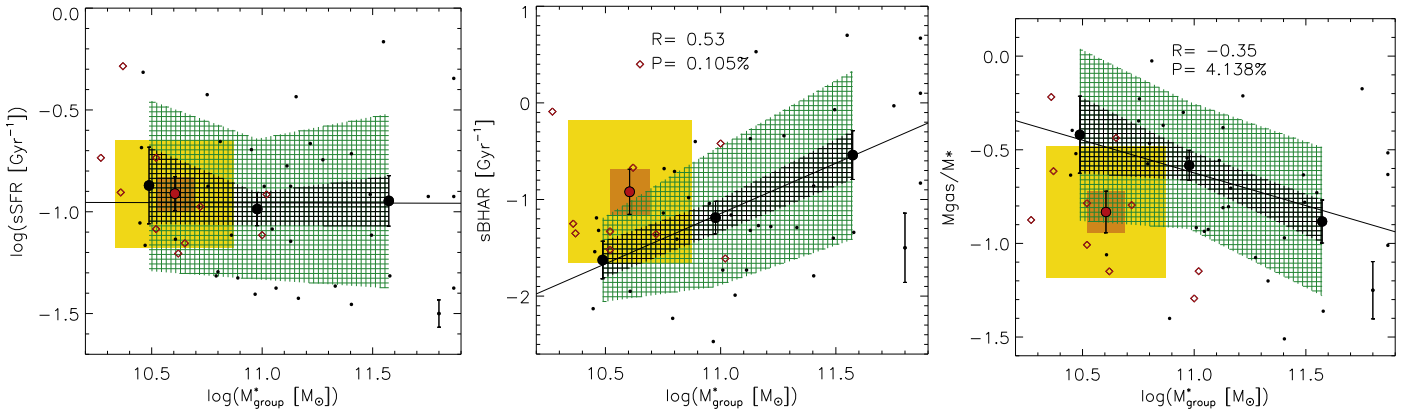


Figure 19. Left panel: sSFR as a function of M_{group}^* at $0.15 < z < 0.3$. No sensible differences are observed between small and bigger groups. Middle panel: sBHAR as a function of M_{group}^* for the same sources. The AGN activity per unit of group mass is higher in more massive groups. Right panel: gas fraction as a function of M_{group}^* . While a decreasing gas fraction is observed toward higher group stellar masses, this dependence is not strong enough to draw definitive conclusions. In all plots, for field galaxies (red squares), the x axis represents the stellar mass M^* of each single galaxy, while for galaxies in groups (black circles), it represents the total stellar mass of the hosting group (M_{group}^*). We consider three bins of M_{group}^* — $M_{\text{group}}^* [M_{\odot}] < 10^{10.75}$, $10^{10.75} < M_{\text{group}}^* [M_{\odot}] < 10^{11.25}$, and $M_{\text{group}}^* [M_{\odot}] > 10^{11.25}$ —but the linear fit (solid line) is computed on the underlying data points, not on the binned data (only galaxies in groups are considered for the fit). The typical uncertainty associated with single data points is reported in the bottom right corner of each plot. These uncertainties are derived from the estimated PDFs of each output parameter of the SED fitting that is required to compute the quantity in the y axis. The correlation coefficient R and the corresponding p -values are reported only when $p < 5\%$.

mentioned above, where all of the kinds of galaxies hosting AGNs (early- and late-type) are considered.

Considering as AGNs only the sources with an IR emission fraction higher than $\log(f_{\text{AGN}}^{5-40}) = -1.7$, as we do in our analysis, the numerical AGN fraction $F_{\text{group}}^{\text{IR}}$ shows weak or no dependence on M_{group}^* (black and red circles in Figure 20). At the same time, the fraction of AGNs in the field ($F_{\text{field}}^{\text{IR}}$) is smaller but still consistent with that measured in groups. Given the relation observed between $\log(f_{\text{AGN}}^{5-40})$ and M_{group}^* (middle panel of Figure 18), we expect this behavior to be dependent on the threshold set for the AGN identification as a consequence of a selection effect. For example, using a higher threshold in f_{AGN}^{5-40} , many of the AGNs in the lowest mass bin would not be identified as such anymore, while the new threshold would not affect the numerical AGN fraction in the highest bin of M_{group}^* by the same measure. Consequently, the use of a higher

threshold in f_{AGN}^{5-40} brings a steeper relation between the numerical AGN fraction and M_{group}^* (Figure 20, yellow and green circles). A similar selection effect is expected if AGNs are selected on the basis of their BHAR (i.e., X-ray emission), given that this quantity also correlates with M_{group}^* in a similar way (Figure 17).

The central BH activity is generally thought to be ignited by nuclear inflows of gas, for example, through galaxy–galaxy mergers (e.g., Barnes & Hernquist 1992; Springel et al. 2005a). Moreover, as observed in Treister et al. (2012), the AGN luminosity strongly correlates with the fraction of host galaxies undergoing a major merger (for $10^{43} < L_{\text{bol}}(\text{erg s}^{-1}) < 10^{46}$). Merging events must be more probable when, in a given volume, the number of galaxies that can potentially merge is higher, such as in small groups.

At the same time, however, Popesso & Biviano (2006) found an anticorrelation between the fraction of AGNs in clusters and

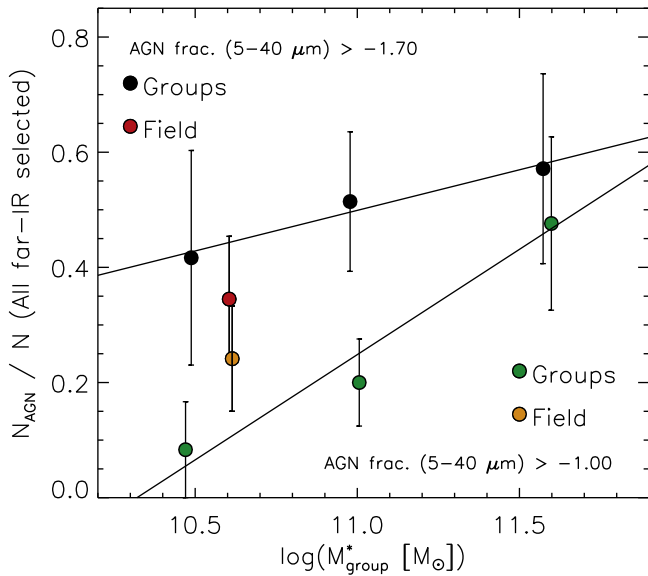


Figure 20. Numerical fraction F^{IR} of AGNs identified at $0.15 < z < 0.3$ using different thresholds in f_{AGN}^{5-40} . In our analysis, only IR-detected sources (MIPS and SPIRE) with $\log(f_{\text{AGN}}^{5-40}) > -1.7$ are identified as AGNs (red circles for $F_{\text{field}}^{\text{IR}}$, black circles for $F_{\text{group}}^{\text{IR}}$). The fraction of AGNs identified slightly increases with M_{group}^* , but given the high uncertainties, it is also consistent with a stable or even declining solution. The use of a higher threshold for the AGN identification (example: $\log(f_{\text{AGN}}^{5-40}) > -1.0$) brings different results (yellow circles for $F_{\text{field}}^{\text{IR}}$, green circles for $F_{\text{group}}^{\text{IR}}$). This different behavior is the result of a selection effect due to the fact that f_{AGN}^{5-40} is an increasing function of M_{group}^* (see left panel of Figure 18).

the velocity dispersion σ_v of the cluster members. The merger rate is found to scale roughly as σ_v^{-3} (Mamon 1992; Makino & Hut 1997). Assuming that the velocity dispersion increases with the mass of the structures (e.g., Heisler et al. 1985; Perea et al. 1990), a similar anticorrelation should be expected between the fraction of AGNs and the total observed stellar mass of the groups. As shown in Figure 20 (black circles), we do not observe such a relation. Our results are more probably consistent with a flat or an increasing $F_{\text{group}}^{\text{IR}}$ at higher M_{group}^* , but given the large uncertainties associated with these estimates, our results do not allow us to exclude the opposite behavior. However, we notice that if the nuclear activity is actually driven by merger events, these must be more probable in richer (i.e., more massive) groups, at least until the velocity dispersion starts to dominate the dynamics of the structures, such as inside galaxy clusters. In any case, we stress the fact that the AGNs in our sample are selected only among star-forming galaxies, while we are not measuring the fraction of AGNs among all of the sources (late star-forming and early-type).

Given these premises, the similar numerical fraction of AGNs identified at all M_{group}^* indicates that the activation of the nucleus of a star-forming galaxy is not more likely in the most massive groups, although, in these cases, the level of nuclear activity is increased, as shown by the BHAR/SFR ratio. As shown in the right panel of Figure 19, the gas fraction of galaxies hosting an AGN tends to be similar or even lower in more massive groups. This observation, together with the similar sSFR measured in low- and high-mass groups, suggests that if a singular infall of gas is responsible for the activation of both AGN and star formation, a higher fraction of this gas must

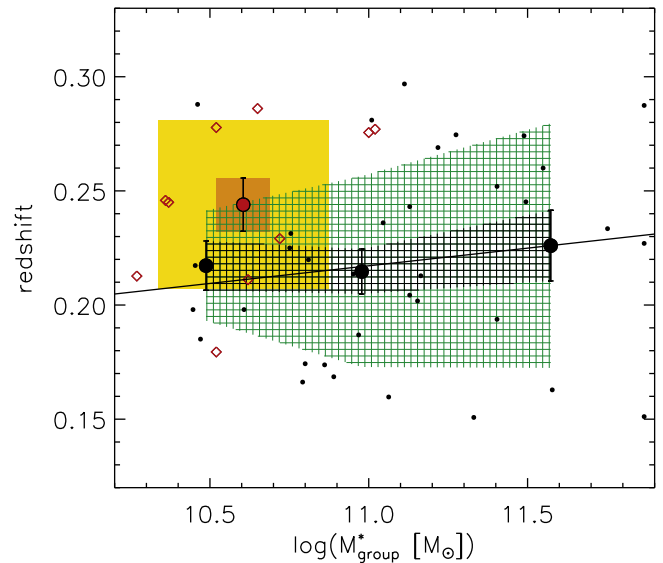


Figure 21. Average redshifts as a function of M_{group}^* . No significant dependence is observed. The higher average redshift observed for field galaxies (in this case, the x axis represents the stellar mass M^* of the single galaxies), although not substantial, could possibly be due to the higher chance to miss group members at higher z .

be driven to the galaxy center if the galaxy is located in a more massive group.

6.2. Selection Effects and Independent Confirmations

In this section, we test the relations found in Section 6.1 against possible biases artificially introduced by our sample selections or the techniques used in our analysis. We also try to find independent confirmations of the same relations.

6.2.1. Completeness of the Groups

Figure 21 shows that the redshift of the group members does not depend on M_{group}^* . This indicates that groups located in the low- z border of the redshift bin that we study ($0.15 < z < 0.3$) are not richer or more complete than those found in the high-redshift border of the same bin. However, field galaxies show higher average redshifts than group members. This could be an effect of the decreasing completeness of the groups at higher redshifts, where the detection of low-luminosity companions, connecting sources in a group through a friends-of-friends algorithm, becomes more difficult. This effect should be particularly prominent for galaxies hosting AGNs, given that in the local universe, their position is usually peripheral with respect to cluster centers (Pimblet et al. 2013). This is particularly true for the most luminous AGNs that avoid high-density regions (Kauffmann et al. 2004). For this reason, the field galaxy sample could possibly be contaminated by group members located at higher redshifts than the average, with an AGN fraction probably higher than the average.

6.2.2. Mid- to Far-IR Flux Ratio

In our analysis, we are considering sources with relatively small AGN emission fractions. These values are not surprising, given that our data sample is made by low-redshift star-forming sources detected above $250 \mu\text{m}$ (i.e., where the emission due to star formation dominates that from the dusty torus of the

AGN). In such a sample, even a particularly IR-bright AGN would bring a relatively small contribution to the total IR emission.

In order to ensure that the relations found are not an artificial effect introduced during the SED fitting process, we measured the ratios between the total mid-IR and total far-IR observed fluxes for the same sources considered in our analysis. We computed the total mid-IR flux ($F_{\text{mid-IR}}$) as the sum of the fluxes measured in all bands that we expect to be more influenced by the AGN torus emission at these low redshifts: 4.5, 7, 11, and 15 μm . For the 11 μm band, we used both the *WISE* W3 and *AKARI* S11 measurements. The fluxes in all bands are normalized using the average flux ratio between the band considered and the W3 band. In a similar way, we computed the total far-IR flux ($F_{\text{far-IR}}$) as the sum of the fluxes measured at 250, 350, and 500 μm . In this case, the 250 μm band is used for the flux normalization.

Figure 22 shows how the behavior of the $F_{\text{mid-IR}}/F_{\text{far-IR}}$ ratio confirms what is found for the AGN emission fractions and BHAR/SFR ratio obtained through the SED fitting (Figure 18). In this case, the p -value of the relation found is higher ($p = 0.7\%$), but this is not unexpected, given that the SED fitting technique is meant to maximize the information obtained from single photometric bands (i.e., it should be more precise). Moreover, the observed fluxes do not take into account the redshifts of the sources, while they are considered in the SED fitting process.

6.2.3. Influence of the M^* –BHAR Relation on Small Groups

As found in Mullaney et al. (2012) and successive works (e.g., Rodighiero et al. 2015), the AGN activity derived from X-ray measurements is related to the stellar mass M^* of each single host galaxy.

In the small-group regime explored in our analysis, we are also considering pairs and triplets. The mass of these groups could easily be dominated by that of the AGNs identified through our selection criteria. In fact, given the M^* –SFR relation (the so-called main sequence), the far-IR selected galaxies in our sample are also the most massive ones. For this reason, the relations that we find with the total mass of the groups could only possibly be apparent and due to the underlying nature of the galaxies considered singularly.

In order to see if the environment plays a real or only an apparent role, we studied the dependence of the AGN emission fraction on the richness of the groups. This parameter is not influenced by the M^* of the selected AGNs. As shown in Figure 23, the AGN emission fraction depends on the total number of group members, similar to what happens with M_{group}^* . This confirms that the relations we find with M_{group}^* are not due to a selection effect. In the same figure, we can broadly identify three different regimes of AGN activity. In very small groups (less than five members), the AGN activity, when detected, is always lower than $\log(f_{\text{AGN}}^{5-40}) = -0.8$ (or -1.5 in the bolometric band). On the other hand, in the richest groups (more than 10 and less than 30 members), the AGN fraction is always higher than the previous limit. Between these two extremes, groups with more than five but less than 10 members show mixed behavior, but with a higher minimum of possible AGN fraction.

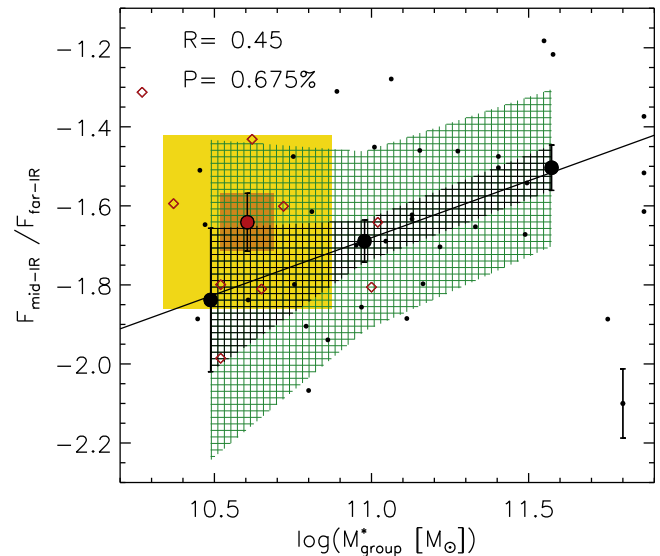


Figure 22. Ratio of total observed mid-IR (4.5, 7, 11, and 15 μm) and far-IR (250, 350, and 500 μm) fluxes as a function of M_{group}^* . The typical uncertainty associated with each single data point is reported in the bottom right corner of the plot. The behavior of the observed fluxes independently confirms what is found using the SED fitting technique.

7. Summary and Conclusions

We presented the multiwavelength catalog of sources detected in the SIMES field. This new catalog, including observations in 30 photometric bands (23, excluding the redundant bands covered by different instruments), is released through the NASA/IPAC IRSA. Our best photo- z estimates are included. Using these photometric data, we studied the AGN emission fraction and the ratio between BHARs and SFRs (BHAR/SFR) for a sample of star-forming galaxies located in the field and in small galaxy groups. The redshift range that we explored goes from $z = 0.15$ to 0.3.

In the mass range $10.25 < \log(M_{\text{group}}^* [M_{\odot}]) < 11.9$, we found that the relative importance of the AGN activity in a star-forming galaxy is an increasing function of the total stellar mass of the hosting group, with $\log(\text{BHAR/SFR}) \propto (1.04 \pm 0.24) \log(M_{\text{group}}^*)$. We suggest that this behavior is due to an increasing efficiency of the BH accretion in larger groups, because the sSFR does not depend on M_{group}^* , while we do observe an increased average sBHAR among more massive groups. The average value of the BHAR/SFR ratio for field AGNs and its dispersion do not allow us to find significant differences between the behavior of field galaxies and galaxies in groups.

Different from the fraction of IR emission due to the central BHs, the numerical fraction of AGNs (i.e., the fraction of sources identified as AGNs in the far-IR selected sample, $F_{\text{group}}^{\text{IR}}$) shows weak or no dependence on M_{group}^* , with the fraction of field AGNs lower but consistent with that measured among group members. However, we found that the slope of this relation depends on the threshold set for the selection of the AGNs: using higher thresholds in f_{AGN}^{λ} (or in BHAR) brings steeper relations between $F_{\text{group}}^{\text{IR}}$ and M_{group}^* . We warn that a similar bias could affect those surveys where AGNs are selected by similar quantities, such as the X-ray emission.

The results summarized here indicate that at these scales, a higher-density environment is more effective in driving a higher rate of nuclear accretion of star-forming galaxies than in

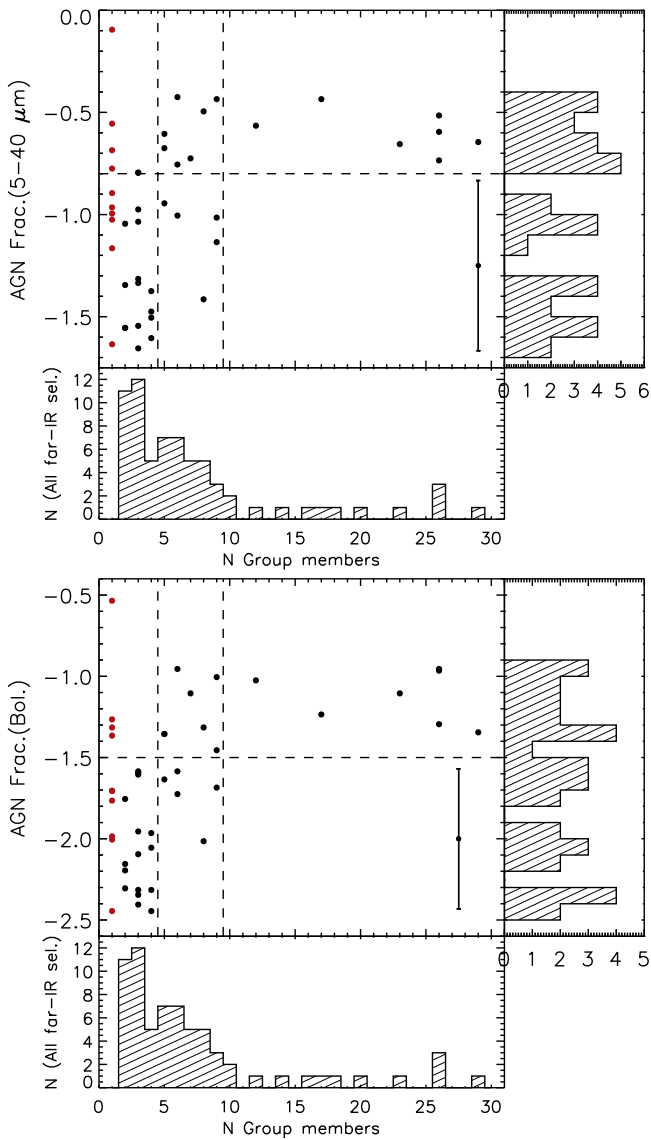


Figure 23. AGN fraction in the 5–40 μm (upper panel) and 8–1000 μm (bottom panel) bands as a function of the richness of the groups. Field galaxies are represented using red filled circles (they are conveniently located at $N = 1$). The typical uncertainty associated with each single data point is reported in the bottom right corner of each plot. These uncertainties are derived from the estimated PDFs of each corresponding output parameter of the SED fitting. We visually delimit two clearly separable regimes of AGN activity using black dashed lines: among the members of the richest groups, the logarithmic AGN fraction (when detected) is always higher than -0.8 and -1.5 in the 5–40 μm and bolometric bands, respectively. On the other hand, very small groups (less than five members) never show an AGN fraction higher than that limit. While the histograms on the right only show the distribution of the sources visible in the plot, the histograms on the bottom show the distribution of all of the far-IR selected galaxies (with and without AGN components).

activating it. In particular, the nuclear accretion is faster if the galaxy is located in a more massive group.

If the AGN activity is driven by merging events (or by gas infall), the chance of an isolated galaxy being subject to such an event must be lower than in a small group. On the other hand, the high velocity dispersion characterizing the richest clusters lowers the probability of these events, as suggested by Popesso & Biviano (2006). The expected net result is AGN activity that increases from low-mass groups toward higher masses until a

turning point is reached, where the velocity dispersion of these structures prevails on the effects of the increased number of possible interactions.

This work is based on observations obtained with *AKARI*, a JAXA project with the participation of ESA; data products from the *Wide-field Infrared Survey Explorer*, which is a joint project of the University of California, Los Angeles, and the Jet Propulsion Laboratory/California Institute of Technology, funded by the National Aeronautics and Space Administration; data from the *Spitzer Space Telescope*, which is operated by the Jet Propulsion Laboratory, California Institute of Technology, under a contract with NASA; data from *Herschel*, an ESA space observatory with science instruments provided by European-led Principal Investigator consortia and with important participation from NASA; and observations made with the *NASA Galaxy Evolution Explorer*, operated for NASA by the California Institute of Technology under NASA contract NAS5-98034. Further fundamental observations were obtained with the ESO VST and VISTA and the CTIO observatories. We gratefully acknowledge Simon Lilly and Alvio Renzini for supplying us with the extended sample of spectroscopic redshifts measured in the COSMOS field. M.V. acknowledges support from the European Commission Research Executive Agency (FP7-SPACE-2013-1 GA 607254), the South African Department of Science and Technology (DST/CON 0134/2014), and the Italian Ministry for Foreign Affairs and International Cooperation (PGR GA ZA14GR02). R.C. acknowledges financial support from CONICYT Doctorado Nacional No. 21161487. I.B. thanks Stefano Rubele for the useful discussions concerning the technical details of the optical data reduction, Lee Armus for his comments on the AGN fraction reliability, and Gabriele Rodeghiero and Maurizio Pajola for their helpful comments about data representation.

ORCID iDs

- I. Baronchelli <https://orcid.org/0000-0003-0556-2929>
 G. Rodighiero <https://orcid.org/0000-0002-9415-2296>
 H. I. Teplitz <https://orcid.org/0000-0002-7064-5424>
 C. M. Scarlata <https://orcid.org/0000-0002-9136-8876>
 S. Berta <https://orcid.org/0000-0002-0320-1532>
 M. Vaccari <https://orcid.org/0000-0002-6748-0577>
 A. Zanella <https://orcid.org/0000-0001-8600-7008>
 C. Mancini <https://orcid.org/0000-0002-4297-0561>
 A. Puglisi <https://orcid.org/0000-0001-9369-1805>
 M. Malkan <https://orcid.org/0000-0001-6919-1237>
 S. Mei <https://orcid.org/0000-0002-2849-559X>
 L. Marchetti <https://orcid.org/0000-0003-3948-7621>
 S. Serjeant <https://orcid.org/0000-0002-0517-7943>
 C. Pearson <https://orcid.org/0000-0001-6139-649X>
 A. Grado <https://orcid.org/0000-0002-0501-8256>
 L. Limatola <https://orcid.org/0000-0002-1896-8605>

References

- Aird, J., Coil, A. L., & Georgakakis, A. 2017a, *MNRAS*, 465, 3390
 Aird, J., Coil, A. L., & Georgakakis, A. 2017b, arXiv:1705.01132
 Alexander, D. M., Bauer, F. E., Brandt, W. N., et al. 2011, *ApJ*, 738, 44
 Alexander, D. M., Smail, I., Bauer, F. E., et al. 2005, *Natur*, 434, 738
 Barnes, J. E., & Hernquist, L. 1992, *ARA&A*, 30, 705
 Barnes, J. E., & Hernquist, L. E. 1991, *ApJL*, 370, L65

- Baronchelli, I., Scarlata, C., Rodighiero, G., et al. 2016a, *ApJS*, **223**, 1
- Baronchelli, I., Scarlata, C., Rodighiero, G., et al. 2016b, *yCat*, **222**
- Berta, S., Lutz, D., Santini, P., et al. 2013, *A&A*, **551**, A100
- Bertin, E., & Arnouts, S. 1996, *A&AS*, **117**, 393
- Béthermin, M., Wang, L., Doré, O., et al. 2013, *A&A*, **557**, A66
- Böhringer, H., Schuecker, P., Guzzo, L., et al. 2004, *A&A*, **425**, 367
- Bolzonella, M., Miralles, J., & Pelló, R. 2000, *A&A*, **363**, 476
- Brammer, G. B., van Dokkum, P. G., & Coppi, P. 2008, *ApJ*, **686**, 1503
- Brinchmann, J., Charlot, S., White, S. D. M., et al. 2004, *MNRAS*, **351**, 1151
- Bruzual, G., & Charlot, S. 2003, *MNRAS*, **344**, 1000
- Burgarella, D., Buat, V., Gruppioni, C., et al. 2013, *A&A*, **554**, A70
- Butcher, H., & Oemler, A., Jr. 1984, *ApJ*, **285**, 426
- Calzetti, D., Armus, L., Bohlin, R. C., et al. 2000, *ApJ*, **533**, 682
- Chabrier, G. 2003, *PASP*, **115**, 763
- Charlot, S., & Fall, S. M. 2000, *ApJ*, **539**, 718
- Ciesla, L., Charmandaris, V., Georgakakis, A., et al. 2015, *A&A*, **576**, A10
- Clements, D. L., Bendo, G., Pearson, D., et al. 2011, *MNRAS*, **411**, 373
- Cowie, L. L., Songaila, A., Hu, E. M., & Cohen, J. G. 1996, *AJ*, **112**, 839
- Coziol, R., Brinks, E., & Bravo-Alfaro, H. 2004, *AJ*, **128**, 68
- Coziol, R., Iovino, A., & de Carvalho, R. R. 2000, *AJ*, **120**, 47
- da Cunha, E., Charlot, S., & Elbaz, D. 2008, *MNRAS*, **388**, 1595
- Daddi, E., Dickinson, M., Morrison, G., et al. 2007, *ApJ*, **670**, 156
- Delvecchio, I., Gruppioni, C., Pozzi, F., et al. 2014, *MNRAS*, **439**, 2736
- Donley, J. L., Koekemoer, A. M., Brusa, M., et al. 2012, *ApJ*, **748**, 142
- Donley, J. L., Rieke, G. H., Rigby, J. R., & Pérez-González, P. G. 2005, *ApJ*, **634**, 169
- Dressler, A., Smail, I., Poggianti, B. M., et al. 1999, *ApJS*, **122**, 51
- Dressler, A., Thompson, I. B., & Shectman, S. A. 1985, *ApJ*, **288**, 481
- Eastman, J., Martini, P., Sivakoff, G., et al. 2007, *ApJL*, **664**, L9
- Eke, V. R., Baugh, C. M., Cole, S., et al. 2004, *MNRAS*, **348**, 866
- Elbaz, D., Daddi, E., Le Borgne, D., et al. 2007, *A&A*, **468**, 33
- Fadda, D., & Rodighiero, G. 2014, *MNRAS*, **444**, L95
- Farrah, D., Afonso, J., Efstathiou, A., et al. 2003, *MNRAS*, **343**, 585
- Farrah, D., Urrutia, T., Lacy, M., et al. 2012, *ApJ*, **745**, 178
- Feltre, A., Hatziminaoglou, E., Fritz, J., & Franceschini, A. 2012, *MNRAS*, **426**, 120
- Fiore, F., Feruglio, C., Shankar, F., et al. 2017, arXiv:1702.04507
- Franceschini, A., Hasinger, G., Miyaji, T., & Malquori, D. 1999, *MNRAS*, **310**, L5
- Fritz, J., De Looze, I., Baes, M., et al. 2016, in *Active Galactic Nuclei: What's in a Name?* (Garching, Germany), **101**
- Fritz, J., Franceschini, A., & Hatziminaoglou, E. 2006, *MNRAS*, **366**, 767
- Genzel, R., Tacconi, L. J., Lutz, D., et al. 2015, *ApJ*, **800**, 20
- Georgantopoulos, I., Comastri, A., Vignali, C., et al. 2013, *A&A*, **555**, A43
- George, M. R., Leauthaud, A., Bundy, K., et al. 2011, *ApJ*, **742**, 125
- Gisler, G. R. 1978, *MNRAS*, **183**, 633
- Grado, A., Capaccioli, M., Limatola, L., & Getman, F. 2012, *MSAIS*, **19**, 362
- Granato, G. L., Silva, L., Danese, L., de Zotti, G., & Bressan, A. 2004, in *Multiwavelength AGN Surveys*, ed. R. Mújica & R. Maiolino (Singapore: World Scientific Publishing Co. Pte. Ltd.), **379**
- Gruppioni, C., Berta, S., Spinoglio, L., et al. 2016, *MNRAS*, **458**, 4297
- Guainazzi, M., Matt, G., & Perola, G. C. 2005, *A&A*, **444**, 119
- Gunn, J. E., & Gott, J. R., III 1972, *ApJ*, **176**, 1
- Hatziminaoglou, E., Fritz, J., Franceschini, A., et al. 2008, *MNRAS*, **386**, 1252
- Hatziminaoglou, E., Fritz, J., & Jarrett, T. H. 2009, *MNRAS*, **399**, 1206
- Heisler, J., Tremaine, S., & Bahcall, J. N. 1985, *ApJ*, **298**, 8
- Hill, J. M., & Oegerle, W. R. 1993, *AJ*, **106**, 831
- Hopkins, A. M., & Beacom, J. F. 2006, *ApJ*, **651**, 142
- Hopkins, P. F., Hernquist, L., Cox, T. J., et al. 2006, *ApJS*, **163**, 1
- Hopkins, P. F., Hernquist, L., Cox, T. J., Robertson, B., & Krause, E. 2007a, *ApJ*, **669**, 67
- Hopkins, P. F., Richards, G. T., & Hernquist, L. 2007b, *ApJ*, **654**, 731
- Huchra, J. P., & Geller, M. J. 1982, *ApJ*, **257**, 423
- Ilbert, O., Salvato, M., Le Floc'h, E., et al. 2010, *ApJ*, **709**, 644
- Iyer, K., & Gawiser, E. 2017, *ApJ*, **838**, 127
- Kauffmann, G., White, S. D. M., Heckman, T. M., et al. 2004, *MNRAS*, **353**, 713
- Kawata, D., & Mulchaey, J. S. 2008, *ApJL*, **672**, L103
- Kennicutt, R. C., Jr. 1998, *ARA&A*, **36**, 189
- Kirkpatrick, A., Pope, A., Alexander, D. M., et al. 2012, *ApJ*, **759**, 139
- Kormendy, J., & Ho, L. C. 2013, *ARA&A*, **51**, 511
- Kron, R. G. 1980, *ApJS*, **43**, 305
- Kurucz, R. 1993, *ATLAS9 Stellar Atmosphere Programs and 2 km/s grid*. Kurucz CD-ROM No. 13 (Cambridge, MA: Smithsonian Astrophysical Observatory), **13**
- Larson, R. B., Tinsley, B. M., & Caldwell, C. N. 1980, *ApJ*, **237**, 692
- Läsker, R., Ferrarese, L., van de Ven, G., & Shankar, F. 2014, *ApJ*, **780**, 70
- Lilly, S. J., Le Fevre, O., Hammer, F., & Crampton, D. 1996, *ApJL*, **460**, L1
- Lilly, S. J., Le Fevre, O., Renzini, A., et al. 2007, *ApJS*, **172**, 70
- Lo Faro, B., Franceschini, A., Vaccari, M., et al. 2013, *ApJ*, **762**, 108
- Lusso, E., Comastri, A., Simmons, B. D., et al. 2012, *MNRAS*, **425**, 623
- Madau, P., Ferguson, H. C., Dickinson, M. E., et al. 1996, *MNRAS*, **283**, 1388
- Magdis, G. E., Daddi, E., Béthermin, M., et al. 2012, *ApJ*, **760**, 6
- Makino, J., & Hut, P. 1997, *ApJ*, **481**, 83
- Mamon, G. A. 1992, *ApJL*, **401**, L3
- Marconi, A., & Hunt, L. K. 2003, *ApJL*, **589**, L21
- Martini, P., Miller, E. D., Brodwin, M., et al. 2013, *ApJ*, **768**, 1
- Martini, P., Sivakoff, G. R., & Mulchaey, J. S. 2009, *ApJ*, **701**, 66
- McCarthy, I. G., Frenk, C. S., Font, A. S., et al. 2008, *MNRAS*, **383**, 593
- McMahon, R. G., Banerji, M., Gonzalez, E., et al. 2013, *MNRAS*, **435**, 35
- Merloni, A., & Heinz, S. 2008, *MNRAS*, **388**, 1011
- Mullaney, J. R., Daddi, E., Béthermin, M., et al. 2012, *ApJL*, **753**, L30
- Noeske, K. G., Faber, S. M., Weiner, B. J., et al. 2007a, *ApJL*, **660**, L47
- Noeske, K. G., Weiner, B. J., Faber, S. M., et al. 2007b, *ApJL*, **660**, L43
- Oliver, S. J., Bock, J., Altieri, B., et al. 2012, *MNRAS*, **424**, 1614
- Onaka, T., Matsuhara, H., Wada, T., et al. 2007, *PASJ*, **59**, 401
- Page, M. J., Symeonidis, M., Vieira, J. D., et al. 2012, *Natur*, **485**, 213
- Park, C., & Hwang, H. S. 2009, *ApJ*, **699**, 1595
- Park, S. Q., Barmby, P., Willner, S. P., et al. 2010, *ApJ*, **717**, 1181
- Perea, J., del Olmo, A., & Moles, M. 1990, *A&A*, **237**, 319
- Pier, E. A., & Krolik, J. H. 1992, *ApJ*, **401**, 99
- Piffaretti, R., Arnaud, M., Pratt, G. W., Pointecouteau, E., & Melin, J.-B. 2011, *A&A*, **534**, A109
- Pimblett, K. A., Shabala, S. S., Haines, C. P., Fraser-McKelvie, A., & Floyd, D. J. E. 2013, *MNRAS*, **429**, 1827
- Poggianti, B. M., von der Linden, A., De Lucia, G., et al. 2006, *ApJ*, **642**, 188
- Polletta, M., Tajer, M., Maraschi, L., et al. 2007, *ApJ*, **663**, 81
- Poppo, P., & Biviano, A. 2006, *A&A*, **460**, L23
- Pozzi, F., Vignali, C., Comastri, A., et al. 2007, *A&A*, **468**, 603
- Pozzi, F., Vignali, C., Gruppioni, C., et al. 2012, *MNRAS*, **423**, 1909
- Richstone, D. O. 1976, *ApJ*, **204**, 642
- Rines, K., Geller, M. J., Kurtz, M. J., & Diaferio, A. 2005, *AJ*, **130**, 1482
- Risaliti, G., & Elvis, M. 2004, in *Supermassive Black Holes in the Distant Universe*, ed. A. J. Barger, **187**
- Rodighiero, G., Brusa, M., Daddi, E., et al. 2015, *ApJL*, **800**, L10
- Rodighiero, G., Daddi, E., Baronchelli, I., et al. 2011, *ApJL*, **739**, L40
- Rodighiero, G., Renzini, A., Daddi, E., et al. 2014, *MNRAS*, **443**, 19
- Saintonge, A., Tran, K.-V. H., & Holden, B. P. 2008, *ApJL*, **685**, L113
- Salpeter, E. E. 1955, *ApJ*, **121**, 161
- Sanders, D. B., Soifer, B. T., Elias, J. H., et al. 1988, *ApJ*, **325**, 74
- Sargent, M. T., Béthermin, M., Daddi, E., & Elbaz, D. 2012, *ApJL*, **747**, L31
- Sedgwick, C., Serjeant, S., Pearson, C., et al. 2011, *MNRAS*, **416**, 1862
- Silva, L., Granato, G. L., Bressan, A., & Danese, L. 1998, *ApJ*, **509**, 103
- Springel, V., Di Matteo, T., & Hernquist, L. 2005a, *ApJL*, **620**, L79
- Springel, V., Di Matteo, T., & Hernquist, L. 2005b, *MNRAS*, **361**, 776
- Tovmassian, H., Plionis, M., & Torres-Papaqui, J. P. 2006, *A&A*, **456**, 839
- Treister, E., Schawinski, K., Urry, C. M., & Simmons, B. D. 2012, *ApJL*, **758**, L39
- Tristram, K. R. W., Meisenheimer, K., Jaffe, W., et al. 2007, *A&A*, **474**, 837
- Tristram, K. R. W., Raban, D., Meisenheimer, K., et al. 2009, *A&A*, **502**, 67
- Turner, M. J. L., Reeves, J. N., Ponman, T. J., et al. 2001, *A&A*, **365**, L110
- Urry, C. M., & Padovani, P. 1995, *PASP*, **107**, 803
- Vaccari, M., Covone, G., Radovich, M., et al. 2017, arXiv:1704.01495
- van den Bosch, F. C., Aquino, D., Yang, X., et al. 2008, *MNRAS*, **387**, 79
- Vasudevan, R. V., & Fabian, A. C. 2009, *MNRAS*, **392**, 1124
- Vega, O., Silva, L., Panuzzo, P., et al. 2005, *MNRAS*, **364**, 1286
- Vika, M., Driver, S. P., Cameron, E., Kelvin, L., & Robotham, A. 2012, *MNRAS*, **419**, 2264
- Wilkes, B. J., Kuraszkiewicz, J., Haas, M., et al. 2013, *ApJ*, **773**, 15
- Williamson, R. A., Hurst, W., & Jeffe, M. 2002, in *ESA Special Publication 515, Space Applications for Heritage Conservation*, ed. B. Warmbein, **15**
- Wright, E. L., Eisenhardt, P. R. M., Mainzer, A. K., et al. 2010, *AJ*, **140**, 1868
- Zacharias, N., Monet, D. G., Levine, S. E., et al. 2005, *yCat*, **1297**, 0